HAL
open science

Environmental cluster effects and galaxy evolution: The H I properties of the Abell clusters A85/A496/A2670

M. M. López-Gutiérrez, H. Bravo-Alfaro, J. H. van Gorkom, C. A. Caretta, F. Durret, L. M. Núñez-Beltrán, Y. L. Jaffé, M. Hirschmann, D. Pérez-Millán

To cite this version:

M. M. López-Gutiérrez, H. Bravo-Alfaro, J. H. van Gorkom, C. A. Caretta, F. Durret, et al.. Environmental cluster effects and galaxy evolution: The H I properties of the Abell clusters A85/A496/A2670. Monthly Notices of the Royal Astronomical Society, 2022, 517, pp.1218-1241. 10.1093/mnras/stac2526 . insu-03839621

HAL Id: insu-03839621

https://insu.hal.science/insu-03839621v1

Submitted on 13 Apr 2023

HAL is a multi-disciplinary open access archive for the deposit and dissemination of scientific research documents, whether they are published or not. The documents may come from teaching and research institutions in France or abroad, or from public or private research centers.

L'archive ouverte pluridisciplinaire **HAL**, est destinée au dépôt et à la diffusion de documents scientifiques de niveau recherche, publiés ou non, émanant des établissements d'enseignement et de recherche français ou étrangers, des laboratoires publics ou privés.

Monthly Notices of the ROYAL ASTRONOMICAL SOCIETY

MNRAS **517,** 1218–1241 (2022)
Advance Access publication 2022 September 8

https://doi.org/10.1093/mnras/stac2526

Environmental cluster effects and galaxy evolution: The HI properties of the Abell clusters A85/A496/A2670

M. M. López-Gutiérrez,[1★] H. Bravo-Alfaro,[1★] J. H. van Gorkom,[2★] C. A. Caretta,[1] F. Durret,[3] L. M. Núñez-Beltrán,[1] Y. L. Jaffé,[4] M. Hirschmann[5,6] and D. Pérez-Millán[1,7]

[1]*Departamento de Astronomía, Universidad de Guanajuato, Guanajuato 36000, Mexico*
[2]*Department of Astronomy, Columbia University, New York, NY 10027, USA*
[3]*Institut d'Astrophysique de Paris, Sorbonne Université, CNRS, UMR 7095, 98bis Bd Arago, F-75014 Paris, France*
[4]*Inst. de Física y Astronomía, Fac. de Ciencias, Universidad de Valparaíso, Avda. Gran Bretaña 1111, Casilla 5030, Valparaíso, Chile*
[5]*Institut de Physique, Laboratoire d'astrophysique, École Polytechnique Fédérale de Lausanne (EPFL), CH-1290 Versoix, Switzerland*
[6]*INAF - Osservatorio Astronomico di Trieste, via G. B. Tiepolo 11, I-34143 Trieste, Italy*
[7]*Instituto de Radioastronomía y Astrofísica, UNAM, Morelia 58089, Mexico*

Accepted 2022 August 24. Received 2022 August 23; in original form 2022 April 7

ABSTRACT

We study the impact of the local environment on the transformation of spiral galaxies in three nearby ($z < 0.08$) Abell clusters: A85/A496/A2670. These systems were observed in HI with the Very Large Array, covering a volume extending beyond the virial radius and detecting 10, 58, and 38 galaxies, respectively. High fractions (0.40–0.86) of bright spirals [$\log(M_*/\mathrm{M}_\odot) = 9-10$] are not detected in H I. We provide further evidence of environmental effects consisting in significant fractions (0.10–0.33) of abnormal objects and a number of red (passive) spirals, suggesting an ongoing process of quenching. Ram-pressure profiles and the sample of the brightest spirals used as test particles for environmental effects indicate that ram-pressure plays an important role in stripping and transforming late-types. Phase-space diagrams and our search for substructures helped to trace the dynamical stage of the three systems. This was used to compare the global cluster effects versus pre-processing, finding that the former is the dominating mechanism in the studied clusters. By contrasting the global distribution of HI normal versus HI disturbed spirals in the combined three clusters, we confirm the expected correlation of disturbed objects located, on average, at shorter projected radii. However, individual clusters do not necessarily follow this trend, and we show that A496 and A2670 present atypical behaviour. In general, we provide conclusive evidence about the dependence of the transformation of infalling spirals on the ensemble of cluster properties like mass, ICM density, dynamical stage, and surrounding large-scale structure.

Key words: galaxies: clusters: individual: Abell 85/496/2670 – galaxies: clusters: intracluster medium – galaxies: evolution.

1 INTRODUCTION

For decades, observations have shown that regions of high galaxy-density, such as cluster cores, are dominated by red E/S0 galaxies, while blue spirals are more abundant in lower density regions. Large amounts of observational evidence have confirmed the *morphology-density relation*, which constitutes one of the clearest pieces of evidence of environment playing an important role in galaxy evolution (Oemler 1974; Dressler 1980; Postman & Geller 1984; Dressler et al. 1997; Goto et al. 2003; Poggianti et al. 2009b). This (*nurture*) scenario is in full agreement with the ΛCDM model of hierarchical formation of structures, where individual galaxies are predicted and observed to follow the stream from low to high-density environments during their lifetime. This galaxy migration seems to be tightly correlated with a systematic change of their physical properties such as morphology, gas content, and SF/AGN activity. On the theoretical side, many works (and references therein; De Lucia, Hirschmann & Fontanot 2019) conclude that secular mechanisms and/or conditions at the time of galaxy formation (*nature*) might be more important than environment in driving galaxy evolution. Theoretical models are still trying to reproduce all the observational trends linked with environment. Nowadays, it is generally accepted that galaxies at low redshifts have been shaped by both nature and nurture. However, the full understanding of the physics behind the galaxy evolution over cosmological timescales remains a very active research field (*e.g.* Peng et al. 2010; Boselli & Gavazzi 2014; Cortese, Catinella & Smith 2021).

Solving the question of morphology transformation of spirals into lenticulars, through an evolutionary sequence involving starburst/post-starburst phases (*e.g.* Boselli & Gavazzi 2006; Barway et al. 2007; Poggianti et al. 2009a; Paccagnella et al. 2017; Boselli, Fossati & Sun 2022), requires the study along two main axes, the environment being one of them. Studying galaxies within the same cosmic epoch but living in different environments helps to find correlations between galaxy properties and the physical conditions of their local environment (Bahé et al. 2013; Spérone-Longin et al. 2021). The second axis corresponds to the cosmic evolution: the study of galaxy properties as a function of redshift has shown that a short ($\leq 10^8$ yr) starburst phase occurs, followed by a long-term

★ E-mail: mm.lopezgutierrez@ugto.mx (MMLG); hector@ugto.mx (HBA); jvangork@astro.columbia.edu (JHvG)

© 2022 The Author(s)
Published by Oxford University Press on behalf of Royal Astronomical Society

Downloaded from https://academic.oup.com/mnras/article/517/1/1218/6694106 by CNRS user on 13 April 2023

and complex quenching process (Rhee et al. 2020; Cortese et al. 2021). As a consequence, the fraction of galaxies in the red sequence almost doubled between $z \sim 1$ and $z = 0$, implying a decrease of blue galaxies accompanied by strong morphology evolution (Butcher & Oemler 1978; Fasano et al. 2000; Arnouts et al. 2007).

Several consortia have been actively approaching the question based on large photometric and spectroscopic surveys such as 2dF and SDSS, covering large sky areas and redshift ranges (Lewis et al. 2002; Balogh et al. 2004; Kauffmann et al. 2004; Poggianti et al. 2017). All these efforts have found indisputable evidence for the impact of environment in galaxy evolution (and references therein; Boselli & Gavazzi 2006, 2014; Cortese et al. 2021). However, understanding the role played by different physical mechanisms exerted under diverse environment conditions constitutes the matter of a very active debate. The involved physical mechanisms are classified in two types: hydrodynamic and gravitational. Hydrodynamic effects concern the stripping of cold/warm interstellar gas (HI and H_2) by the hot intracluster medium (ICM). The ram-pressure stripping (RPS, Gunn & Gott 1972) and the viscous stripping (Nulsen 1982) are the most studied cases. On the other side, we have the tidal (gravitational) mechanisms occurring between a galaxy and the cluster potential (Byrd & Valtonen 1990) or among neighbour galaxies (Merritt 1983; Barnes & Hernquist 1996; Walker, Mihos & Hernquist 1996). These include major mergers, accretion of low-mass satellites, and the accumulation of fast speed encounters between galaxies (the *galaxy harassment*, Moore, Katz & Lake 1996). The removal of the galaxy halo gas, known as galaxy starvation (*e.g.* Larson, Tinsley & Caldwell 1980), is predicted to occur either by hydrodynamic or gravitational interactions. Most of these mechanisms are predicted to transform a spiral galaxy into an S0, and it is known that more than one process might act simultaneously on a single galaxy. The *pre-processing* of galaxies occuring within groups infalling towards clusters and seems to be particularly important (Donnari et al. 2021). Groups of galaxies are known to have lower velocity dispersions than clusters, allowing slower and deeper tidal interactions among their members. Several authors (Fadda et al. 2008; Poggianti et al. 2009b) provided substantial evidence that strong galaxy evolution is occurring in low-mass systems at a large distance from the cluster core. However, the debate *pre-processing* versus *cluster effects* remains open because many variables are involved, such as the infalling orbits, initial gas/stellar masses, the group/cluster properties, and even the surrounding large-scale structure (Rhee et al. 2020; Salerno et al. 2020).

In this context, studying the atomic hydrogen (HI) of spiral galaxies, in combination with observations at other frequencies and with numerical simulations, has proven to be a powerful tool to study galaxy evolution as a function of environment. HI is probably the best tracer of galaxy interactions as it extends well beyond the stellar disc. Several studies have been devoted to the nearest clusters such as Virgo, Hydra, A 1367, and Coma (*e.g.* Giovanelli & Haynes 1985; Cayatte et al. 1990; Bravo-Alfaro et al. 2000; Solanes et al. 2001; Chung et al. 2009; Scott et al. 2010, 2018; Boselli et al. 2021; Wang et al. 2021; Molnár et al. 2022). The large coverage and highly sensitive HI-surveys carried out with single dish telescopes, such as HIPASS and ALFALFA (Giovanelli et al. 2005; Haynes et al. 2018), provided statistical information on the HI content of large samples of spirals in different environments. All these surveys have shown that spirals in clusters have systematically less gas than their counterparts in the field. This loss of cold gas is known to be the first step to the eventual quenching of star formation observed in cluster galaxies.

In parallel to single-dish surveys, HI synthesis imaging provides critical information mainly at low redshifts. This technique unveils different types of disruptions like gas shrunk discs, asymmetries, and offsets between the gas and the stellar discs (and references therein Bravo-Alfaro et al. 2001; Chung et al. 2009; Scott et al. 2018; Luber et al. 2022). HI-maps and kinematical velocity fields are essential to constrain hydrodynamical simulations of galaxies under different environment processing (*e.g.* Vollmer et al. 2012; Tonnesen 2019, and references therein). With a few remarkable exceptions, HI-synthesis imaging surveys are restricted to the nearby universe ($z < 0.1$) due to instrumental limitations and to the very long observing times required. As a consequence, only a few clusters have been fully covered by using this technique. The new generation of radio telescopes such as ASKAP and MeerKAT (Jonas & MeerKAT Team 2016; Koribalski et al. 2020), as well as upgraded instruments like the Westerbork Synthesis Radio Telescope (WSRT) and the Karl G. Jansky Very Large Array (VLA), are nowadays pushing farther the redshifts of HI-imaged galaxies. The BUDHIES project (Jaffé et al. 2013, 2016; Gogate et al. 2020) uses the WSRT to characterize the HI properties in and around two clusters at $z = 0.2$, A963, and A2192. The CHILES project (Fernández et al. 2013; Hess et al. 2019) uses the VLA to image the HI in a 40 arcmin field out to $z = 0.45$ and has made a direct detection at the largest distance so far, at $z = 0.376$ (Fernández et al. 2016). In parallel to pushing the study of HI to higher redshifts (the *time axis*), it is equally important to enlarge the sample of studied clusters lying at the same epoch (the *environment axis*). Large-volume, HI-blind imaging surveys like the one presented in this work are intended to explore different clusters from their core to the outskirts. The HI maps and kinematics of resolved objects are studied as a function of the very diverse environments where galaxies are located.

In this paper, we enlarge the sample of nearby systems ($z < 0.08$) imaged in HI. Large volumes of the Abell clusters A85, A496, and A2670 were homogeneously observed with the VLA. We discuss their global HI properties, paying special attention to a complete sample of bright spirals, used as test particles for environment effects. We obtain HI physical parameters of individual galaxies and deliver an atlas of HI maps and velocity fields. Bright spirals not detected in HI are of particular interest. We seek for correlations between gas properties of individual galaxies within the substructures reported in this work as a test quantifying the pre-processing. We present profiles of the ram pressure and projected phase space diagrams (PPS) for each cluster. Finally, we use the gas content and colour index as a first approach to quantify the quenching fraction in the studied clusters. In forthcoming papers, we will use optical spectra and multiband observations to complement the study of individual galaxies, in particular those showing strong distortions in HI and in optical.

This paper is organized as follows: Section 2 describes the clusters under study, the observations, and the data reduction for the HI and the optical imaging. In the same section, we describe the catalogues of member objects used in this work, as well as the sample of the brightest spirals and the colour–magnitude diagrams of the studied clusters. In Section 3, we give the main observational results: we provide the HI parameters of all detected galaxies and their global distribution across the observed clusters. Tables containing these data and the corresponding HI maps are given in the Appendix. In Section 4, we study the dynamical state of the three clusters by applying two independent methods tracing substructures. In Section 5, we calculate RPS profiles and we obtain radial velocity versus cluster-centric distance plots in order to study the assembly history of the clusters. In Section 6, we compare the clusters with each other and we discuss the role played by the cluster environment in the evolution of infalling galaxies. We summarize our results and

Downloaded from https://academic.oup.com/mnras/article/517/1/1218/6694106 by CNRS user on 13 April 2023

Table 1. Properties of the studied clusters.

	A85	A496	A2670
RA (2000)	00 41 50	04 33 38	23 54 14
Dec. (2000)	−09 18 07	−13 15 33	−10 25 08
z/D_c (Mpc)	0.055/233	0.033/140	0.076/320
D_l (Mpc)	245.4	144.9	344.1
scale 10 arcmin (Mpc)	0.69	0.41	0.95
v_{cl} (km s^{-1})	16607	9884	22 823
σ_{cl} (km s^{-1})	1054	685	781
R_{200} (Mpc)	2.54	1.68	1.86
M_{200} (10^{14} M$_\odot$)	12.6	3.49	5.07
Morph (B-M)	I	I	I-II
Richness	130	134	224
L_X (10^{44} erg^{-1})	9.4	3.8	2.3
LSS	SC (11)	isolated(∗)	isolated

Notes:
–D_c (comoving distance), D_l (luminosity distance), and linear scale for 10 arcmin are estimated with $H_0 = 70$ km s^{-1}Mpc^{-1}.
–The central velocity (v_{cl}), the velocity dispersion (σ_{cl}) and L_X were taken from NED, HyperLeda and BAX, respectively.
–R_{200}: computed following Finn et al. (2005).
–M_{200} was estimated following Barsanti et al. (2018).
–LSS (large scale structure): indicates that A85 is part of the supercluster MSCC 039, consisting of 11 cluster members (Chow-Martínez et al. 2014).
(∗) We revisit the LSS of A496 in this work.

give our conclusions in Section 7. Throughout this paper we assume $\Omega_M = 0.3$, $\Omega_\Lambda = 0.7$, and $H_0 = 70$ km s^{-1}Mpc^{-1}.

2 THE OBSERVATIONS

2.1 The cluster sample

In this work, we study the Abell clusters A85 ($z = 0.055$), A496 ($z = 0.033$), and A2670 ($z = 0.076$), which harbour different physical properties (see Table 1) and dispose of ancillary multifrequency data.

A85 is more massive and more luminous in X-rays than the other two systems. Despite its relaxed morphology, it is known to be undergoing minor merging processes with a subcluster and groups seen in X-rays and in the optical (Durret et al. 1998; Durret, Lima Neto & Forman 2005; Bravo-Alfaro et al. 2009). More recently, this system has been confirmed to possess a centrally peaked profile in X-rays with a sloshing pattern (Ichinohe et al. 2015) and with some additional disturbed features (Laganá, Durret & Lopes 2019). The presence of jellyfish galaxies like JO201 has been associated with strong RPS in this cluster (Ramatsoku et al. 2020; Luber et al. 2022, and references therein).

A496 is known to have a very relaxed morphology (Durret et al. 2000; Boué et al. 2008a; Ulmer et al. 2011), consistent with a significant coincidence between the BCG and the cluster centroid (position and velocity) (Lopes et al. 2018). Nevertheless, Laganá et al. (2019) reported disturbed features superposed on to a centrally peaked X-ray distribution. Concerning the LSS, A496 was reported as an isolated system by Chow-Martínez et al. (2014). We revisit this result in Section 6.

A2670 is the faintest of the three systems in X-rays; however, its ICM is not negligible: RPS is blamed for strong sweep of material observed in a post-merger galaxy (Sheen et al. 2017). A2670 is the most irregular of the three systems and displays a very elongated morphology distributed along a NE-SW axis. This cluster is dynamically young, as suggested by the diffuse X-ray emission and the large offset in velocity of 333 km s^{-1} (Caretta, private communication) between the cluster and the BCG; this clearly indicates that the massive galaxy has not yet settled at the bottom of the cluster potential well.

Table 2. HI observational parameters.

ID	T_{int} (h)	VLA config.	beam (arcsec)	Bandw MHz	Correl. mode
(1)	(2)	(3)	(4)	(5)	(6)
A85	80	C	24 × 17	6.3	2AC
A496	12	C	25 × 17	6.3	2AC
A2670	90	C	23 × 16	12.5	1A, 1D

Notes. Column (2): The time on source, in hours.
Column (3): The VLA configuration used.
Column (4): The beam size in arcsec.
Column (5): The applied bandwidth in MHz.
Column (6): The correlator mode.

2.2 The HI data

We take advantage of HI-data obtained with the VLA[1] between 1994 and 1996 for A2670, and from 2001 to 2003 for A85 and A496. All observations were taken in C configuration, producing beam sizes of ∼ 24 × 17 arcsec^2. Table 2 gives the main observing parameters: the total integration time, the VLA configuration, the beam size, the bandwidth, and the correlator mode applied. The correlator mode defines the number of polarizations applied. The correlator mode 1 uses one polarization and allows a larger number of velocity channels; mode 2 applies two polarizations and is able to produce an improvement in sensitivity by a factor of $\sqrt{2}$. Hanning smoothing was used on the data of A85 and A496, obtaining a set of 31 independent channels. For A2670, no Hanning smoothing was applied, obtaining a set of 63 channels (cubes NE and SW). The general observing strategy is based on a combination of several observing pointings at different positions and central velocities. This allowed to cover the full cluster volume beyond one virial radius and more than three times the velocity dispersion. Fig. 1 shows the total observed fields for each cluster, and Table 3 gives the parameters of the final HI data cubes. Throughout this paper, we list the HI heliocentric velocities using the optical definition.

We applied different observing strategies to each cluster depending on their redshifts and velocity dispersions. Six VLA fields were pointed side by side across A85. The individual fields have slight overlap in RA, Dec. in order to avoid any gap in between. These fields have the same central velocity giving a homogeneous coverage across an area of ∼100 arcmin side after a mosaicing procedure (Taylor, Carilli & Perley 1999). The same six fields were observed three times, each centred at a different velocity: 15 266, 16 500, and 17 744 km s^{-1} (see Table 3). The central velocities were chosen to slightly overlap producing a homogeneous coverage of some 3800 km s^{-1}, i.e. more than 3.5 times the velocity dispersion of A85.

A similar procedure was applied to A496. Since it is located at two-thirds the distance of A85 the total integration time for A496 was significantly reduced. On the other hand this cluster is spread across a larger region of the sky and we had to apply ten VLA pointings

[1]The National Radio Astronomy Observatory is a facility of the National Science Foundation operated under cooperative agreement by Associated Universities, Inc.

Downloaded from https://academic.oup.com/mnras/article/517/1/1218/6694106 by CNRS user on 13 April 2023

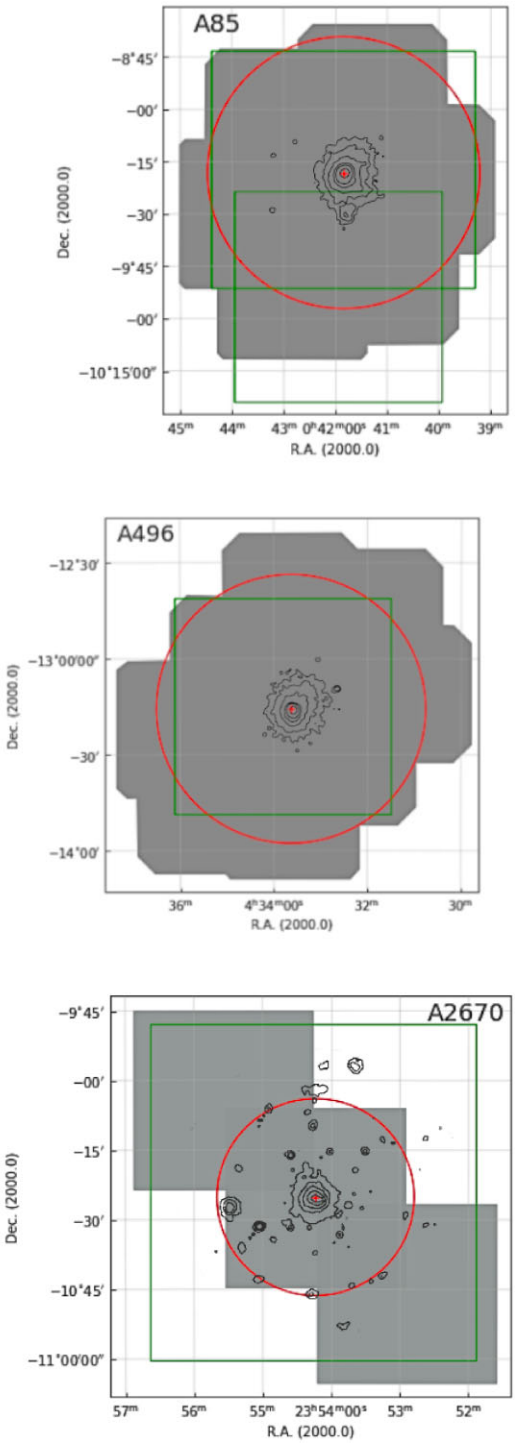

Figure 1. The observed fields in HI (grey polygons) and in optical (green squares). A85 is in the top panel, A496 in the middle, and A2670 in the bottom. The R_{200} radius is indicated with a red circle and the black contours draw the *ROSAT* X-ray emission. The BCG is indicated with a red cross.

with different RA, Dec. positions in order to reach the one virial radius coverage. These fields went through a mosaicing procedure delivering a field of view of some 100 arcmin. Having a low-velocity dispersion (737 km s^{-1}), the ten fields were observed two times, each one centred at a different velocity: 9285 and 10 429 km s^{-1}. This delivered a coverage of $\sim$ 2400 km s^{-1}, equivalent to more than 3.5 times the cluster velocity dispersion (Table 3).

A different observing strategy was applied to A2670. Located at a larger distance than the previous clusters, A2670 needed fewer VLA pointing fields to cover the virial radius. However, due to its distance, longer observing time was needed in order to reach a similar detection limit as the other clusters. The one-virial-radius coverage was ensured by pointing three VLA fields spread along a NE–SW axis and having some overlap in order to avoid any gaps. Due to observing time limitations, the covered area is elongated, giving priority to the NE-SW axis. Mosaicing was not applied in this cluster, and the three data cubes were analysed separately. The velocity coverage was ensured by applying a bandwidth of 12.5 MHz and correlator modes 1A for the central cube, and 1D for the NE and SW cubes. This strategy delivered a central data cube with a coverage of 4000 km s^{-1} and nearly 3000 km s^{-1} for the NE and SW cubes (Table 3).

Standard VLA calibration and imaging were carried out by using the NRAO Astronomical Image Processing System (AIPS). All final data cubes for A85 and A496 have 31 channels with velocity widths of between 43.8 and 46.9 km s^{-1}. The central field A2670-C has 88 channels, while 2670-NE and 2670-SW have 63 channels. All data cubes for this cluster have a channel width close to 48 km s^{-1}. The imaging was made by applying `ROBUST`= 1.0 (Briggs 1995), which is the best compromise between uniform and natural weighting. This maximizes the sensitivity while keeping high-spatial resolution, delivering a final beam size of about 24 $\times$ 17 arcsec^2 for the three clusters. The typical rms is $\sim$ 0.24 mJy beam^{-1} for A85 and A496, while $\sim$0.12 mJy beam^{-1} was reached for A2670 (see Table 3). This allowed us to obtain HI-mass detection limits of the same order of magnitude for the three systems.

The search for detections and the HI analysis was carried out using AIPS. The moment maps were produced with the AIPS task MOMNT, and applied with Gaussian (space coordinates) and Hanning smoothing (velocity) to maximize the signal-to-noise ratio (S/N). We produced HI-maps and velocity fields using a cutoff level between 1.5 and 2.0 times the rms measured in the corresponding data cube. As expected, variations of noise were found at the edge of the data cubes, in RA, Dec., and velocity. We normally discarded detections found within those zones.

2.3 CFHT MegaCam optical images

We obtained optical images with the 3.6m Canada–France–Hawaii Telescope and the MegaCam instrument, each field having a size of around 1 $\times$ 1 deg^2. The south tip and the infalling filament of A85 were observed in October 2004 (programme 04BF02); we exploit here the *u g r i* band images, with surface magnitude limits of 26.7, 27.3, 26.4, and 25.7 mag arcsec^{-2}, respectively. Details can be found in Boué et al. (2008b). We later retrieved archive images, this time centred on A85 in the *g* and *r* bands. The corresponding depths are 26.3 and 26.1 mag arcsec^{-2}. We assembled the individual images (five in each band) to obtain frames with total exposure times of 3960 s and 8380 s.

A496 was observed with the same telescope and instrument (November 2003, programme 03BF12) obtaining *u g r i* band images. The total exposure time is 7853 s for each image and the depths are 27.4, 27.2, 26.2, and 25.6 mag arcsec^{-2}, respectively. Details on these data can be found in Boué et al. (2008a).

Downloaded from https://academic.oup.com/mnras/article/517/1/1218/6694106 by CNRS user on 13 April 2023

Table 3. The HI-data cubes.

Data cube (1)	RA (2000) (2)	Dec (2000) (3)	FoV (arcmin) (4)	Vel. range km s^{-1} (5)	V_c km s^{-1} (6)	Δv km s^{-1} (7)	rms mJy beam^{-1} (8)	M_{HI} limit 10^8 M$_\odot$ (9)
A85–LV	00 41 51.9	−09 18 17	90	1366	15266	45.5	0.25	9.0
A85–MV	00 41 51.9	−09 18 17	90	1330	16500	46.9	0.25	9.2
A85–HV	00 41 51.9	−09 18 17	90	1387	17744	46.2	0.25	9.1
A496–LV	04 33 04.1	−13 06 19	100	1314	9285	43.8	0.24	3.0
A496–HV	04 33 04.1	−13 06 19	100	1324	10429	44.2	0.24	3.0
A2670–C	23 54 13.8	−10 25 09	40	4120	23037	47.9	0.11	7.9
A2670–NE	23 55 34.1	−10 04 18	40	2957	22690	47.7	0.12	8.6
A2670–SW	23 52 53.4	−10 46 00	40	2957	22690	47.7	0.12	8.6

Notes. Column (1): Field ID, where LV, MV, and HV indicates low, medium, and high velocity ranges, respectively.
Columns (2) and (3): Central coordinates for the data cube, after mosaicing for A85 and A496.
Column (4): Approximate diameter of the FoV, in arcmin.
Column (5): Total velocity coverage, in km s^{-1}.
Column (6); The heliocentric velocity of the central channel, using the optical definition.
Column (7): Velocity resolution given by the channel width, in km s^{-1}.
Column (8): The rms per channel in mJy beam^{-1}.
Column (9): The HI-mass detection limit, in units of 10^8 M$_\odot$.

The data for A2670 were taken from the CFHT archive, with a total exposure time of 6160 s in the *u g r z* bands. The depths are 25.7, 26.8, 26.3, and 24.2 mag arcsec^{-2}, respectively.

2.4 The membership catalogues

We use the spectroscopic redshift compilation by Andernach (private communication) to define the member sample of the three clusters. This compilation considers as potential members all galaxies with published radial velocities inside a projected Abell radius ($R_A = 2.1\,h_{70}^{-1}$ Mpc), and within a range of ∼2500 km s^{-1} from a preliminary estimation of the cluster velocity. Several observational limitations could prevent the redshift catalogues to be fully complete within the studied regions, but nevertheless, it remains the most reliable option with the data currently available in the literature. Taking this redshift sample, the membership catalogues are constructed by tracing caustic curves representing the escape velocity of the system in a projected phase-space diagram (see, Serra et al. 2011, and references therein for more details). The curves are constructed following Chow-Martínez (2019). All galaxies within the defined limits are taken as cluster members. The caustics applied here are intentionally *relaxed* (an enclosing fit) as the catalogues are intended to retain as many potential member galaxies as possible. The membership catalogues contain 616, 368, and 308 objects in A85, A496, and A2670, respectively. Due to its larger redshift, A2670 is sampled through a larger linear radius. This bias will be taken into account when we compare the observed clusters with each other in Section 6.

2.5 Catalogue of the brightest spiral galaxies

HI blind surveys covering large cluster volumes allow to study the gas component of all the member galaxies contained within the observed data cubes. Even those spirals not detected in HI are very important as they trace the distribution of HI swept spirals throughout the studied cluster. With this in mind we built catalogues (RA, Dec., and $v_{\rm rad}$) of the brightest spirals contained within the VLA data cubes. As a first step, magnitudes *g* and *r* were obtained for all the member galaxies by applying SExtractor (Bertin & Arnouts 1996) to the CFHT images referred above. A few zones observed by the VLA but not covered by the CFHT (Fig. 1) were similarly analysed by using Pan-STARRS frames (Flewelling et al. 2020).

The strategy to define the bright spiral catalog is as follows. We applied a limit in apparent magnitude of $g = 19.0$, 18.0, and 19.5, for A85, A496, and A2670, respectively. Considering the distance to each cluster, these values roughly correspond to the same absolute magnitude, $M_g \sim -18.0$. In *r* band this limit is close to $M_r = -18.2$. We convert these magnitudes to stellar mass following Mahajan et al. (2018), showing that our catalogues of bright spirals are complete in mass above a value of $\log(M_*/\mathrm{M}_\odot) = 9.0$. We did not apply a colour-index threshold in order to include any possible red spiral. This method delivered bright objects whose morphology can be defined through visual inspection; this was done by using combined (RGB) optical images from CFHT and Pan-STARRS. All objects in the blue cloud (see next subsection) and having a stellar mass above $\log(M_*/\mathrm{M}_\odot) = 9.0$ were considered as candidates to be spiral. Our visual inspection confirmed spiral features for most of those objects. The remaining ones, before being included in the sample of bright spirals, should present a combination of features based on a disky shape, blue $(g - r)$ colour, stellar mass, HI content, and the presence of dust lanes (for the near edge-on ones). As shown below, a few red spirals are reported in the three clusters. Their belonging to the bright spiral sample was conditioned by the following criteria: having a mass above $\log(M_*/M_\odot) = 9.0$, being detected in HI or, alternatively, showing spiral features through our visual inspection. This output was cross-matched with the list of member objects (Section 2.4) in order to ensure that these spirals are cluster members. The final catalogues of bright spirals consist of 65, 46, and 61 member objects in A85, A496, and A2670, respectively. Hereafter, we denote these objects as B-Sp.

2.6 Colour–magnitude diagrams: the galaxy populations

Tracing colour–magnitude diagrams (CMD) in a cluster helps to visualize the distribution of different types of galaxies populating the system. Fig. 2 shows the CMD of the three clusters, giving the colour index as a function of the absolute magnitude M_r (bottom axis) and stellar mass (upper axis). The red dotted line draws the border between the red sequence and the green valley; it is defined as: $(g - r) = 0.63 - 0.02\,(M_r + 20)$ (Masters et al. 2010).

Downloaded from https://academic.oup.com/mnras/article/517/1/1218/6694106 by CNRS user on 13 April 2023

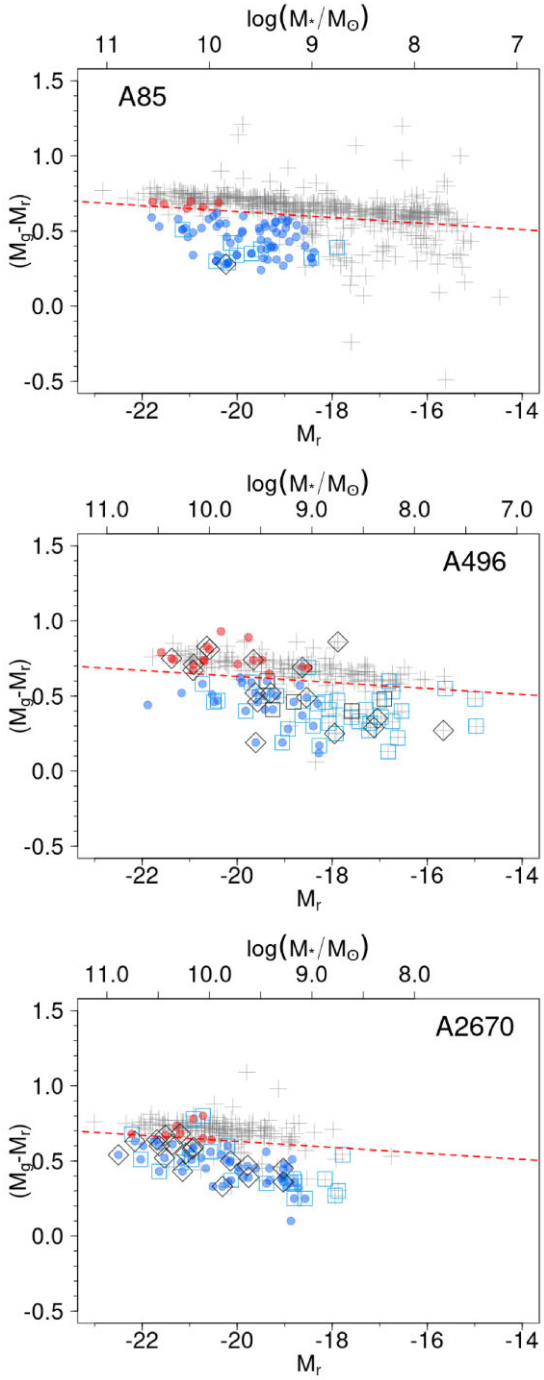

Figure 2. Colour–magnitude diagrams showing cluster members with grey crosses. The red dotted line draws the border between the red sequence and the green valley (see text). The bright spirals are shown with solid circles (blue and red). Squares/diamonds indicate the HI normal/abnormal galaxies (see Section 3).

Member galaxies in Fig. 2 are shown with grey crosses. The bright spirals defined in the previous section are cluster members too; they are indicated with solid circles, either red or blue, indicating their position in the red sequence or in the blue cloud. Cluster members in the red sequence being brighter than $M_r = -18.2$ (i.e. mass above $\log(M_*/\mathrm{M}_\odot) = 9.0$), and having no solid circle, correspond to early types.

Galaxies above the same mass limit and lying in the blue cloud are confirmed to be part of the B-Sp sample (see previous subsection). The HI detections are shown with blue open squares (normal objects) or with black diamonds (HI-abnormal objects, defined in the next section). A few HI detections are not part of the compilation of member galaxies; either no redshift was available or they are outside the velocity window defined by the membership catalogue in Section 2.4. We added these objects as new cluster members.

Galaxies located in the blue clouds of these clusters are good candidates to be in a pre-quenching stage. Optical colours are not the best indicators for current star-forming activity due to possible differences between the time scales for quenching and for the change in colour due to the stop of star formation. Nevertheless, not having optical spectra for all the objects under study, we consider that a blue colour combined with a normal gas content, constitute a reasonable indicator for galaxies in a pre-quenching phase. On the other side, objects above the red line of Fig. 2 are not expected to have any intense star formation activity, therefore red circles in this figure constitute very likely passive spirals. A *K*-correction was applied to the three clusters. The largest *K*-correction values in colour-index are slightly above 0.1 mag. As expected, these values correspond to red objects in A2670 (we used the *K*-correction calculator from GAISh[2]). As this correction is associated with the galaxy distance, the *y*-axis of Fig. 2 shows the difference in absolute magnitudes after the *K*-correction was applied. Galactic extinction is negligible for these clusters, and no correction was applied.

3 RESULTS

3.1 The HI detected galaxies

The catalogues of bright spirals (B-Sp) described above provide positions and velocities that were used to seek for their HI-emission in the corresponding data cubes. Most of these B-Sp were effectively detected in HI but, in all three clusters, significant fractions of these spirals were not detected. These objects constitute our sample of HI-non-detected spirals. This sample is complete in mass above the limit $\log(M_*/M_\odot) = 9.0$. The search for 21 cm emission was completed by a thorough visual inspection of the HI data cubes. This was done blindly, disregarding all information on optical positions and redshifts of the spiral galaxies. Our search produced a list of emissions, most of which matching in position and velocity with a B-Sp. However, several candidate detections had no counterpart in the B-Sp Catalogue. A subsequent search upon the optical-RGB frames and redshift catalogues allowed the finding of the optical counterparts. As expected, these are blue, irregular galaxies, fainter than the limit defining the B-Sp sample.

Our strategy to search for HI-emitting galaxies includes a conservative detection threshold above 6 times the rms, delivering 10, 58, and 38 HI-detections in A85, A496, and A2670, respectively. A few HI objects are just marginally resolved by the VLA primary beam: two in A85, six in A496, and eleven in A2670. All maps and velocity fields are available as online material. We used the HI mass detection limits given in Table 3 to ensure that the sample of bright spirals (Section 2.5) is potentially detected with this survey. Obviously, more massive spirals have higher chances to be detected than less massive ones. Therefore, we inspect the performance of our survey detecting galaxies with different stellar masses. We displayed our

[2]This research made use of the 'K-corrections calculator' service available at http://kcor.sai.msu.ru

Downloaded from https://academic.oup.com/mnras/article/517/1/1218/6694106 by CNRS user on 13 April 2023

HI mass detection threshold on to a $M_{\rm HI}$ versus M_* plot (not shown in this work). We added the scaling relation obtained by Dénes, Kilborn & Koribalski (2014) and we found that normal galaxies can be effectively detected down to $\log(M_*/{\rm M}_\odot) = 9.0$. The deeper data cubes in A496 pushed this limit down to $\log(M_*/{\rm M}_\odot) = 8.7$. This confirms that our full sample of B-Sp can be detected with the present survey under unperturbed conditions.

Tables A1–A3 give the main optical and HI-parameters of the detected galaxies in A85, A496, and A2670, respectively. The lists of non-detected spirals are given in Tables B1–B3 for the same clusters. Five HI detections in A496 could not be properly measured as we did not recover their full emission; this is due to limited velocity coverage of the corresponding data cube. We consider these galaxies as HI detections because the recovered emission has a large S/N; they are indicated with black squares in Figs 2 and 3.

In Tables A1–A3, the first five columns give names, coordinates and morphological type; these data are taken from the literature (NED[3] and HyperLEDA[4]). Columns 6 and 7 give optical magnitudes and $(g - r)$ colours obtained from CFHT and from Pan-STARRS images. In Column (8) we provide the stellar masses obtained from our M_r magnitudes. Columns (9) and (10) give the optical and HI velocities, the latter in heliocentric frame. We consider the value of the central channel displaying emission as the HI velocity. We give the HI velocity width in Column (11) defined by the full range of channels containing emission; this constitutes a proxy for W_{20}. The HI mass (Column 12) in solar masses is calculated by using the equation:

$$\left[\frac{M_{\rm HI}}{{\rm M}_\odot}\right] = 2.36 \times 10^5 \cdot \left[\frac{D_c}{\rm Mpc}\right]^2 \cdot \left[\frac{S_{\rm HI}}{\rm Jy\ km\ s^{-1}}\right], \quad (1)$$

where we use the corresponding comoving distance ($D_{\rm c}$) for all the members of the same system. The uncertainty for $M_{\rm HI}$ is systematically $\leq$ 10 per cent, derived from the computed error on the total flux $S_{\rm HI}$. The HI-deficiency is estimated with the equation (Haynes & Giovanelli 1984)

$$Def_{\rm HI} = log(M_{\rm HI})_{\rm exp} - log(M_{\rm HI})_{\rm obs}. \quad (2)$$

Given that only a reduced number of our galaxies has reliable morphological types in the literature, we computed the $Def_{\rm HI}$ parameter for the two cases proposed by Haynes & Giovanelli (1984), i.e. for early-spirals and late-spirals. These values can be taken as the lower and upper limits (Columns 13 and 14) of the deficiency parameter. Column (15) gives the projected distance to the cluster centre, using the BCG position. In Column (16), we provide a code indicating four different kinds of disruptions observed in HI; this helps to define the sub-sample of HI abnormal galaxies. The codes given in this column are the following:

(i) *N* : galaxies with normal HI content and distribution.

(ii) *Def* : indicates galaxies having lost more than 50 per cent of their gas ($Def_{\rm HI} \gtrsim 0.25$).

(iii) *Asy* : denotes a resolved HI asymmetry, or a tail, unveiled by the HI maps.

(iv) *Pos* : indicates an offset $\geq$ 20 kpc in position, between the HI and optical centroids; this limit roughly corresponds to the diameter of a typical spiral and is equivalent to 19, 30, and 14 arcsec, for A85, A496, and A2670, respectively.

[3]The NASA/IPAC Extragalactic Database (NED) is operated by the Jet Propulsion Laboratory, California Institute of Technology, under contract with the National Aeronautics and Space Administration.

[4]The HyperLeda database available at http://leda.univ-lyon1.fr/

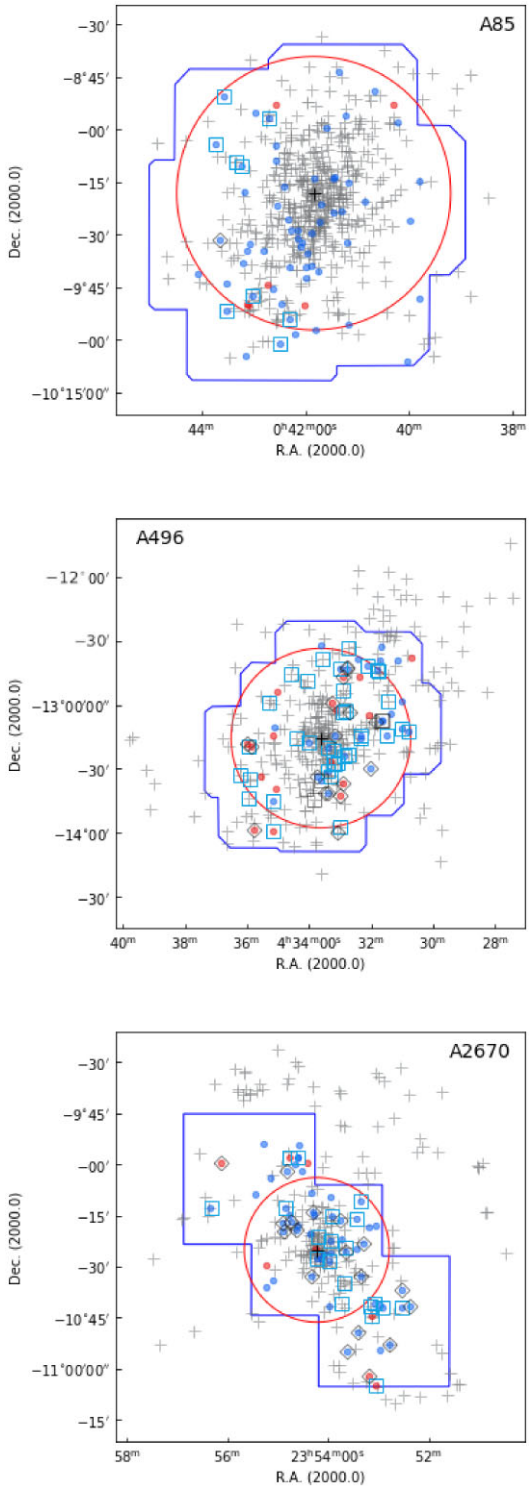

Figure 3. The distribution of member galaxies (grey crosses) in the studied clusters. HI detections are shown with blue squares (normal) and black diamonds (abnormal). Symbols for the bright spirals are the same as in Fig. 2 (blue and red circles). R_{200} is indicated with a red circle, and the blue polygon shows the VLA field of view. The cluster centre is indicated with a red cross.

Downloaded from https://academic.oup.com/mnras/article/517/1/1218/6694106 by CNRS user on 13 April 2023

(v) *Vel* : denotes a velocity offset between the optical and HI velocities; we use three times the HI channel width to define this offset ($\sim$135 km s^{-1}).

Galaxies having at least one of the four criteria mentioned above are defined as HI abnormal. We used this sub-sample of perturbed objects to carry out a search for a correlation between HI-deficiency and HI-asymmetry, finding no obvious trend. However, this result based on gas deficient yet HI detected galaxies must be taken with caution as these objects are caught at an early stripping phase. We have no information on the two-dimensional (2D) gas distribution of the even more stripped spirals, i.e. those not detected in HI. Therefore, a deficiency–asymmetry correlation, developing during later gas stripping stages, should not be discarded *a priori*.

3.2 Global distribution of HI across the studied clusters

Some of our main results are displayed in Figs 3 and 4 and in Table 4. The (RA, Dec) distribution of member galaxies in the three studied clusters is shown in Fig. 3. We use the same symbols as in Fig. 2 in order to emphasize the position of the bright spirals (blue/red circles) and the HI detected galaxies (open blue squares/black diamonds). The total fields covered with the VLA are drawn by blue polygons and the corresponding R_{200} are indicated with red circles.

Fig. 4 shows the moment-zero HI-maps of the detected galaxies in each cluster. Galaxies are set at their proper location and are magnified by a factor of five for clarity. We use a colour code in order to separate these galaxies in three radial velocity regimes: lower, similar, and larger than the cluster velocity. We give statistical significance to the velocity slots by applying the same criteria as Wang et al. (2021), given as a function of the velocity dispersion of the cluster ($\sigma_{\rm cl}$) given in Table 1: blue colour for $\Delta v_{\rm rad} < -0.5\sigma_{\rm cl}$, green for $-0.5\sigma_{\rm cl} < \Delta v_{\rm rad} < 0.5\sigma_{\rm cl}$, and red for $0.5\sigma_{\rm cl} < \Delta v_{\rm rad}$. The X-ray emission is shown in grey scale taking advantage of the homogeneous and large field map given by *ROSAT*.

Table 4 reports the total number of objects having different observational properties and lying in specific cluster regions. Data are displayed as follows: Row (1) gives the full number of cluster members, including the new members derived from the HI velocities. Row (2) provides the number of galaxies within the VLA FoV. Rows (3) and (4) give the total number of HI detections and bright spirals. Rows (5), (6), and (7), give the number of B-Sp being HI detected, the B-Sp non-detected, and the B-Sp lying in the red sequence, respectively. Rows (8), (9), and (10), give the number of galaxies detected in HI lying in the red sequence, the HI abnormal, and those below the limit $\log(M_*/{\rm M}_\odot) = 9.0$, respectively. The last three rows, (11), (12), and (13), provide the number of galaxies projected within the virial region (Section 5.2) being: cluster members, bright spirals, and HI detections, respectively. The data given in Table 4 are not well suited for a direct comparison of the clusters with each other because of their different redshifts and VLA coverage. We carry out a comparison under homogeneous conditions in Section 6.

3.2.1 *The HI in Abell 85*

Fig. 3 (upper panel) shows the distribution of 616 member galaxies in A85, where the solid circles indicate the 65 B-Sp. The blue open squares and one black diamond indicate the ten HI detected objects. The cluster members (grey crosses) are rather homogeneously distributed across A85, while the B-Sp and the HI detected galaxies show a very asymmetric distributions across the cluster. The SE zone has more bright spirals than all the other quadrants taken together; all

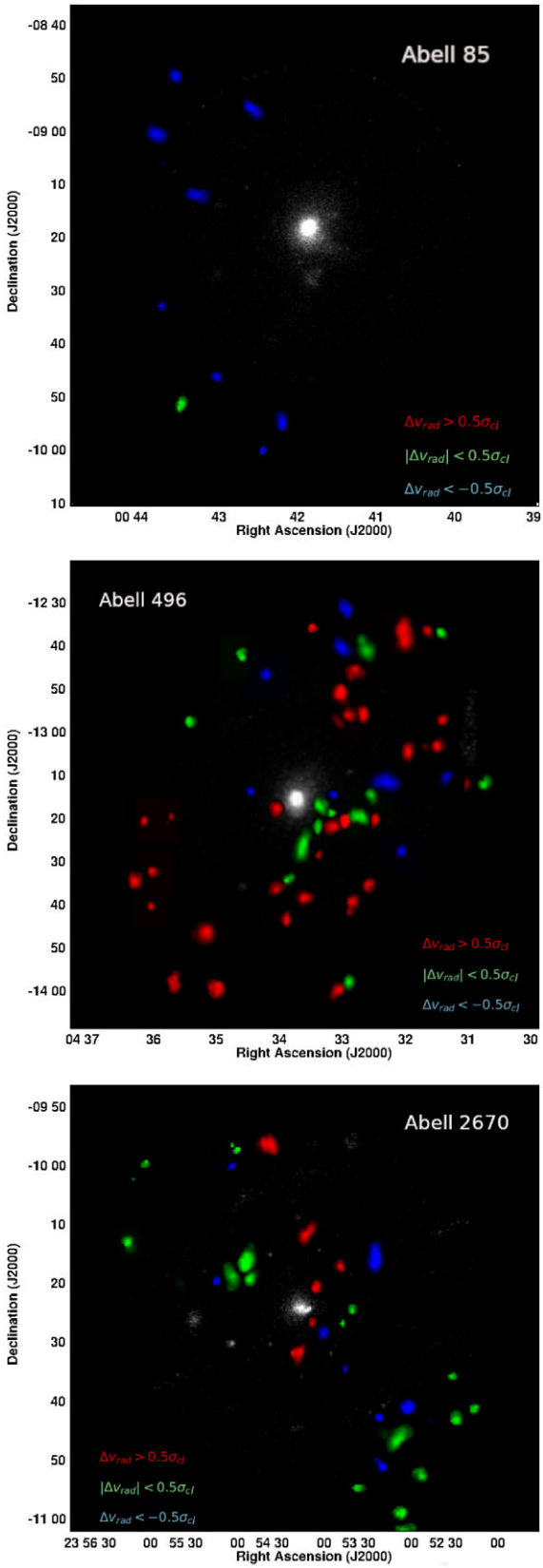

Figure 4. The distribution of HI detected galaxies in A85 (top), A496 (middle), and A2670 (bottom). These objects are separated in three slices of velocity relative to the cluster centre (see text). The HI maps are enlarged by a factor of 5. The *ROSAT* X-ray emission is shown in grey scale.

Downloaded from https://academic.oup.com/mnras/article/517/1/1218/6694106 by CNRS user on 13 April 2023

Table 4. Different types of galaxies in the studied clusters.

	Sample	A85	A496	A2670
(1)	Members	616	383	318
(2)	Memb. VLA-FoV	603	336	254
(3)	HI-det	10	58	38
(4)	B-Sp	65	46	61
(5)	B-Sp HI-det	9	29	33
(6)	B-Sp HI non-det	56	17	28
(7)	B-Sp in red seq	6	17	8
(8)	HI-det in red seq	0	11	5
(9)	HI-det abnormal	1	17	18
(10)	HI-det low mass	1	28	4
(11)	Memb. virial-region	140	203	108
(12)	B-Sp virial-region	23	20	17
(13)	HI-det virial-region	1	24	12

the HI-detections are projected as well on to the SE–NE regions (Figs 3 and 4). The gas-rich galaxies are projected 1.5–3.0 Mpc away from the cluster centre, while a remarkable absence of HI detections at lower radius suggests the presence of a harsh environment. This fact is independently supported by the presence of strongly perturbed galaxies (Venkatapathy et al. 2017; Ramatsoku et al. 2020; Luber et al. 2022).

The sample of 65 B-Sp in A85 is unexpectedly high. A significant fraction of these objects are projected around the cluster core and in the transition zone between the centre and the SE (Fig. 3). Six B-Sp are reaching the red sequence (red solid circles in Fig. 2) and none of them is detected in HI, indicating that they have gone through an advanced stripping process. On the contrary, all the galaxies detected in HI show very blue colours indicating that they have not gone through any stripping phase.

The asymmetry in the distribution of HI-detections is even more striking in Fig. 4, showing that all but one detections are in the low-velocity domain, with a narrow Δv of $\sim$15 000–15 200 km s^{-1} (see Table A1). Their low-velocity dispersion and the large difference compared with the systemic velocity of A85 ($\sim$1 500 km s^{-1}) suggest that they could share a common origin.

3.2.2 *The HI in Abell 496*

The middle panel of Fig. 3 shows the distribution of 383 member galaxies in A496, with 46 B-Sp and 58 galaxies detected in HI (symbols are the same as in Fig. 2). A first remarkable difference of A496 when compared with A85 is given by the lower number of bright spirals (46 in A496, and 65 in A85) but a much larger number of HI-detections (58 in A496 for only 10 in A85; see Table 4). Interestingly, $\sim$50 per cent of the HI detected galaxies in A496 correspond to gas-rich, low mass objects which are not part of the B-Sp sample, i.e. their stellar mass is below $\log(M_*/\mathrm{M}_\odot) = 9.0$. This fraction is partly explained by A496 being closer than the other studied clusters. However, we will show that some peculiarities remain after considering the observational bias due to the difference in redshift.

The distribution of HI detected objects in A496 (Fig. 3) is striking, with many HI-normal galaxies projected on to the central regions. The middle panel of Fig. 4 helps solve the paradox: the objects with low-velocity relative to the cluster (maps in green, in the velocity range $-0.5\sigma_{\rm cl} < \Delta v_{\rm rad} < 0.5\sigma_{\rm cl}$) could be dominated by a movement on the plane of the sky, with circular orbits still far from the densest ICM regions (Dressler 1986). The sample of red maps projected close to the cluster core in Fig. 4 has large components of velocity along the line of sight. They must be at an early stage of infalling, accounting for their normal gas content.

Seventeen B-Sp in A496 are found in the red sequence; eleven of them still retain enough gas to be detected, some are classified as HI abnormal and are indicated with black diamonds in Figs 2 and 3. This strongly suggests that they are under an advanced process of stripping. Most of the red spirals in A496 are projected in the NW and SE quadrants; in Section 6, we discuss a possible relation between their gas properties and their location within the cluster.

3.2.3 *The HI in Abell 2670*

The bottom panel of Fig. 3 shows the distribution of 315 member galaxies in A2670, emphasizing the position of 61 bright spirals and 38 HI-detections (same symbols as previous figures). From the 61 B-Sp reported in this cluster, 28 are not detected in HI, suggesting an active sweeping process. Fig. 2 shows eight B-Sp in the red sequence, some of them retaining enough gas to be detected in HI.

Fig. 3 unveils a complex distribution of the HI detections in A2670, which are mostly projected on to the cluster core and to the SW. Most of the HI non-detected bright spirals in A2670 (solid blue/red circles without square or diamond in Fig. 3), are located near the core and to the NE. Fig. 4 shows a trend of abundant HI-rich galaxies in the SW while the NE beyond 1 R_{200} is very poor in HI. The centre shows a balance between shrunk and extended HI maps, but we remind that strong projection effects might be present in this zone.

4 CLUSTER SUBSTRUCTURE ANALYSIS

In order to get a better understanding of the assembly history of the studied clusters, we carried out a search for substructures based on two independent methods: the tests proposed by Dressler & Shectman (1988) and Serna & Gerbal (1996). For the two tests, we applied the compilation of member galaxies described in Section 2. In general, we have found large coincidences with the two methods. The detected substructures are shown in Fig. 5, and they will be used, in combination with the positions of HI abnormal galaxies, as a test for pre-processing (Section 6).

4.1 Substructures: the Δ-test

We applied an improved version of the well-known Δ-test (Dressler & Shectman 1988), which is based on the parameter-δ, defined by:

$$\delta^2 = \frac{N_{nn}+1}{\sigma_{\rm cl}^2}[(v_{\rm local}-v_{\rm cl})^2 + (\sigma_{\rm local}-\sigma_{\rm cl})^2], \quad (3)$$

where $v_{\rm cl}$ and $\sigma_{\rm cl}$ are the cluster global parameters, and $v_{\rm local}$ and $\sigma_{\rm local}$ are the local parameters calculated for every galaxy relative to its $N_{\rm nn}$ nearest neighbours. In this work, we assume $N_{\rm nn} = 10$; modifying this parameter does not significantly change our results (Bravo-Alfaro et al. 2009).

The Δ-test detects a substructure as a concentration of galaxies showing high values of the parameter-δ; this has proven to be a reliable tracer of substructures. However, this method loses some accuracy in certain cases, for instance, when two groups at different distances from the observer are projected along the same LOS. In this case, the Δ-test will produce one single overestimation of the parameter-δ, detecting only one structure. This is critical in the absence of a dominating large structure, like in bimodal/multimodal systems. In order to improve this method we introduce dividing surfaces on a 3D distribution of RA, Dec., and $v_{\rm loc}$. This separates

Downloaded from https://academic.oup.com/mnras/article/517/1/1218/6694106 by CNRS user on 13 April 2023

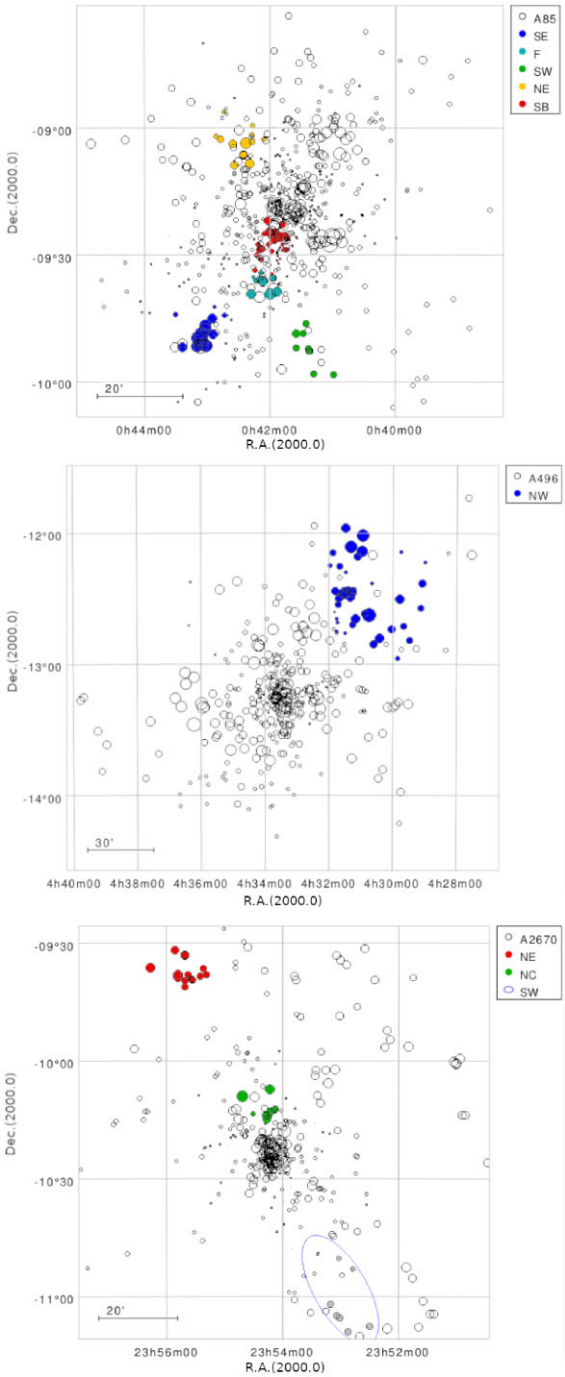

Figure 5. Substructures detected with the Δ-test. Sizes of the circles grow with the probability to belong to a substructure. Coloured circles are part of the extracted groups. (Top panel): In A85 all but one substructure (the NE) are detected as well with the Serna–Gerbal method. (Middle panel): The Δ-test for A496 unveiled one large substructure to the NW. The Serna–Gerbal test found no substructures in this cluster. (Bottom panel): The Δ-test in A2670 detected two substructures, the NC and NE. The Serna–Gerbal test unveiled these two groups plus a third group in the SW, indicated with a blue ellipse.

the sub-groups of galaxies that share the same kinematic properties within their particular caustics, but somehow detached from the kinematics of the whole cluster. That is, we do not take into account only the parameter-δ, but also the $v_{\rm loc}$ and the phase-space distribution of galaxies that are candidates to be members of the substructures (more details in Caretta et al. in preparation). Values of the parameter-δ are illustrated in Fig. 5 by black circles; these circles grow with the probability of a galaxy belonging to a group. Individual values of the parameter-δ will be available upon request.

4.1.1 Δ-test results in A85

We revisit the analysis of substructures of A85 (Bravo-Alfaro et al. 2009) by taking advantage that the number of redshifts for member galaxies has grown significantly in the last years (*e.g.*, Boué et al. 2008b). For the full sample of cluster members, we report a velocity dispersion of $\sigma_v = 1054\,{\rm km\,s^{-1}}$. We report the following substructures.

(i) The main cluster body, with 532 galaxies, has a central velocity $v = 16\,650\,{\rm km\,s^{-1}}$, and $\sigma_v = 1092\,{\rm km\,s^{-1}}$.

(ii) The South-East (SE) substructure, with 15 members, has $v = 15\,157\,{\rm km\,s^{-1}}$, and $\sigma_v = 298\,{\rm km\,s^{-1}}$.

(iii) The *Filament* group *F*, with 10 objects, $v = 15\,840\,{\rm km\,s^{-1}}$, and $\sigma_v = 372\,{\rm km\,s^{-1}}$; this and the SE substructures did not change significantly, compared with previous works, as only few new redshifts are provided for these regions.

(iv) The Southern Blob (SB) is better defined than in previous articles; it has 38 members, $v = 16\,947\,{\rm km\,s^{-1}}$, and $\sigma_v = 282\,{\rm km\,s^{-1}}$.

(v) An interesting difference compared with previous works is the C2 substructure (see Fig. 4 of Bravo-Alfaro et al. 2009) which has lost its signal because the dominant object, the jellyfish galaxy KAZ-364 (also known as JO201), lies slightly outside of the caustic contours. This galaxy is outside the velocity range of our HI cubes, so it is not included in the present analysis. Despite a velocity of ∼3000 km s^{-1}, relative to the cluster, Bellhouse et al. (2017) reported this object as a fast, infalling cluster member being part of a small group.

(vi) We unveiled two new low-mass substructures (< 2 per cent of the total number of member galaxies); the first is at the south-West with 9 galaxies, $v = 16\,236\,{\rm km\,s^{-1}}$, and $\sigma_v = 183\,{\rm km\,s^{-1}}$.

(vii) Another new substructure lies to the NE with 12 galaxies, having $v = 16\,345\,{\rm km\,s^{-1}}$, and $\sigma_v = 300\,{\rm km\,s^{-1}}$.

4.1.2 Δ-test results in A496

We detected a main cluster body with 330 galaxies and a $\sigma_v = 674\,{\rm km\,s^{-1}}$. We clearly unveiled one single substructure located ∼1° (2.5 Mpc) NW from the cluster centre, with 38 members (above 10 per cent of the total mass), $v = 9338\,{\rm km\,s^{-1}}$, and $\sigma_v = 457\,{\rm km\,s^{-1}}$ (see Fig. 5). Our HI survey covers only a small portion of that group, delivering only limited information on the cold gas associated with this structure.

4.1.3 Δ-test results in A2670

We obtained the following results for A2670:

(i) The main cluster body emerges with 287 members, $v = 22\,806\,{\rm km\,s^{-1}}$, and $\sigma_v = 805\,{\rm km\,s^{-1}}$.

(ii) We unveiled two low-mass structures, the first one projected close to the centre (NC, ∼10 arcmin to the north) with 7 members, $v = 22\,883\,{\rm km\,s^{-1}}$, and $\sigma_v = 20\,{\rm km\,s^{-1}}$. This velocity suggests a merger with the main cluster body.

(iii) The NE group lies ∼50 arcmin (4.5 Mpc), NE from the cluster centre, with 14 members, $v = 23\,115\,{\rm km\,s^{-1}}$, and $\sigma_v = 424\,{\rm km\,s^{-1}}$ (Fig. 5). This structure is just north of the VLA FoV (Fig. 3), and we do not dispose of HI information for these galaxies.

Downloaded from https://academic.oup.com/mnras/article/517/1/1218/6694106 by CNRS user on 13 April 2023

4.2 Substructures: the Serna–Gerbal test

In parallel to the Δ-test described above, we applied the Serna–Gerbal (S–G) method (Serna & Gerbal 1996) to the three clusters. This test introduces a fundamental, independent element to detect substructures: the relative potential energies of each pair of galaxies by using individual galaxy brightness as a proxy for the stellar mass. We use the *r*-band magnitude for this goal. In practice the S–G test requires an input catalogue of positions, velocities, magnitudes (converted to masses assuming a value of M/L), and a defined number n of galaxies needed to build a group. We used $n = 10$ as a representative value. The S–G test works hierarchically, seeking for lower level substructures within a primary (more massive) detected group. This delivers an output list of galaxies belonging to each substructure and provides the mass of the corresponding group. Absolute masses of individual structures are not highly accurate, but the relative masses of the groups, normalized to the total member sample, are very reliable.

4.2.1 S–G results in A85

The S–G programme computed for A85 a mass of $M_{\rm tot} = 6.51 \times 10^{14}\,{\rm M}_{\odot}$ for the entire cluster, and a velocity dispersion of $\sigma_{tot} = 1037\,{\rm km\,s^{-1}}$. The S–G test detected the main cluster body (identified as #1) with 587 galaxies, a relative mass $M_1 = 0.792\,M_{\rm tot}$, and $\sigma_1 = 949\,{\rm km\,s^{-1}}$. A secondary group (#2) is detached from the main cluster body, lying south from the centre and having 21 galaxies, $M_2 = 0.079\,M_{\rm tot}$, and $\sigma_2 = 184\,{\rm km\,s^{-1}}$. This structure is coincident with the SB group detected by the Δ-test.

In the next step, we took Structure #1 as the starting point, and we unveiled two further substructures; the first one (identified as #1.1) has 144 galaxies with $M_{1.1} = 0.218\,M_{\rm tot}$, and $\sigma_{1.1} = 527\,{\rm km\,s^{-1}}$. Some galaxies from this group account for the SE subcluster, detected as well with the Δ-test. The second substructure (#1.2) has 14 galaxies, a relative mass $M_{1.2} = 0.01\,M_{\rm tot}$, and $\sigma_{1.2} = 180\,{\rm km\,s^{-1}}$. Finally, the group #1.1 harbours two additional substructures: the first (#1.1.1) has 74 galaxies with $M_{1.1.1} = 0.125\,M_{\rm tot}$, and $\sigma_{1.1.1} = 481\,{\rm km\,s^{-1}}$. This group coincides in position with the minor SW structure obtained with the Δ-test. Another dozen galaxies from the structure #1.1.1 emerge as a group lying between the SB and the *Filament*, unveiling a more complex region, south of the core, than what is shown by the Δ-test. A final subgroup (#1.1.2) appears with 10 galaxies, a relative mass of $M_{1.1.2} = 0.009\,M_{\rm tot}$ and $\sigma_{1.1.2} = 173\,{\rm km\,s^{-1}}$. This substructure matches with the *Filament* group detected with the Δ-test. With the exception of the NE group, the S–G test successfully confirmed the substructures found with the Δ-test in A85.

4.2.2 S–G results in A496

We analysed the full sample of member galaxies, but we found no major substructures in A496. Even modifying the parameter n (for instance with $n = 5$) we did not find significantly different results. The S–G method finds that A496 is a relaxed cluster with negligible substructuring, in agreement with previous studies (*e.g.* Boué et al. 2008a).

4.2.3 S–G results in A2670

In the first step, the S–G test detected two groups in A2670. The largest structure (#1) has 123 galaxies with a σ_v comparable to that of the entire cluster, having $M_1 = 0.490\,M_{\rm tot}$. The second group (#2) has 10 galaxies, a mass $M_2 = 0.016\,M_{\rm tot}$, and $\sigma_{\#2} = 215\,{\rm km\,s^{-1}}$. Group (#2) is placed ∼40 arcmin SW from the cluster centre and was not detected by the Δ-test (see Fig. 5). Very interestingly, this substructure embraces the zone where several HI-rich galaxies are reported (see bottom panel of Fig. 4). These objects have similar physical properties (position, velocity, gas richness), giving further support for this group to be real.

In a second run, the large structure (#1) is decomposed into two substructures (#1.1 and #1.2) having 83 and 11 galaxies, respectively. The former contains $M_{1.1} = 0.270\,M_{\rm tot}$, and a velocity dispersion comparable to that of the cluster. The group #1.2 contains $M_{1.2} = 0.180\,M_{\rm tot}$, and $\sigma_{1.2} = 433\,{\rm km\,s^{-1}}$. The fact that the substructures #1 and #1.1 present high σ_v, comparable to that of the whole cluster, reduces the statistical significance for these groups, as shown by Serna & Gerbal (1996). However, part of substructure #1.1 extends from the centre to the north, coinciding with the *NC* group found with the Δ-test. The same occurs with substructure #1.2, coinciding with the *NE* group, reinforcing the existence of these two groups (Fig. 5).

The two methods, the Δ-test and the Serna–Gerbal, confirm the very complex substructure system of A85, contrasting with the very low level shown by A496. The two tests show A2670 as an intermediate case with a few, not very massive substructures.

Table 5. Parameters of the ICM model.

	A85	A496	A2670
r_c (kpc)	82	30	174
ρ_0 (cm^{-3})	0.0257	0.0407	0.00383
β	0.532	0.484	0.700

Notes: Parameters for A85 and A496 are taken from Chen et al. (2007). We followed Cirimele, Nesci & Trèvese (1997) for A2670.

5 RAM PRESSURE AND PHASE-SPACE DIAGRAMS

With the aim of studying the effects exerted by the ICM on the cold gas content of individual galaxies, we compute the ram-pressure stripping (RPS) profiles for the three studied clusters and compare them with different values of the anchoring force (see the review by Boselli et al. (2022) for further details.) Next, we build and analyse the PPS diagrams for each cluster, displaying the position of all member galaxies.

5.1 Ram pressure stripping in A85, A496, and A2670

In order to estimate the RPS radial profiles, we follow the theoretical definition proposed by Gunn & Gott (1972), $RPS = \rho_{\rm ICM} \times v_{\rm rel}^2$. Here $\rho_{\rm ICM}$ is the local density of the intracluster medium, and $v_{\rm rel}$ is the galaxy velocity relative to the ICM. We estimate the ICM density ($\rho_{\rm ICM}$) as a function of the cluster radius by applying the hydrostatic-isothermal β-model of Cavaliere & Fusco-Femiano (1976), $\rho(r) = \rho_0[1 + (r/r_c)^2]^{-3\beta/2}$. Table 5 gives the parameters of the β-model for the studied clusters: the core radius r_c, the central density ρ_0 and the β value used to calculate the density as a function of the cluster radius. The corresponding RPS profiles are shown in Fig. 6 where we display three representative velocities, which are multiple values of the velocity dispersion of each cluster: $0.66\sigma_{\rm cl}$ in blue, $1.0\sigma_{\rm cl}$ in green, and $1.5\sigma_{\rm cl}$ in red. This adds physical meaning to the comparison of the RPS intensity among different clusters.

Downloaded from https://academic.oup.com/mnras/article/517/1/1218/6694106 by CNRS user on 13 April 2023

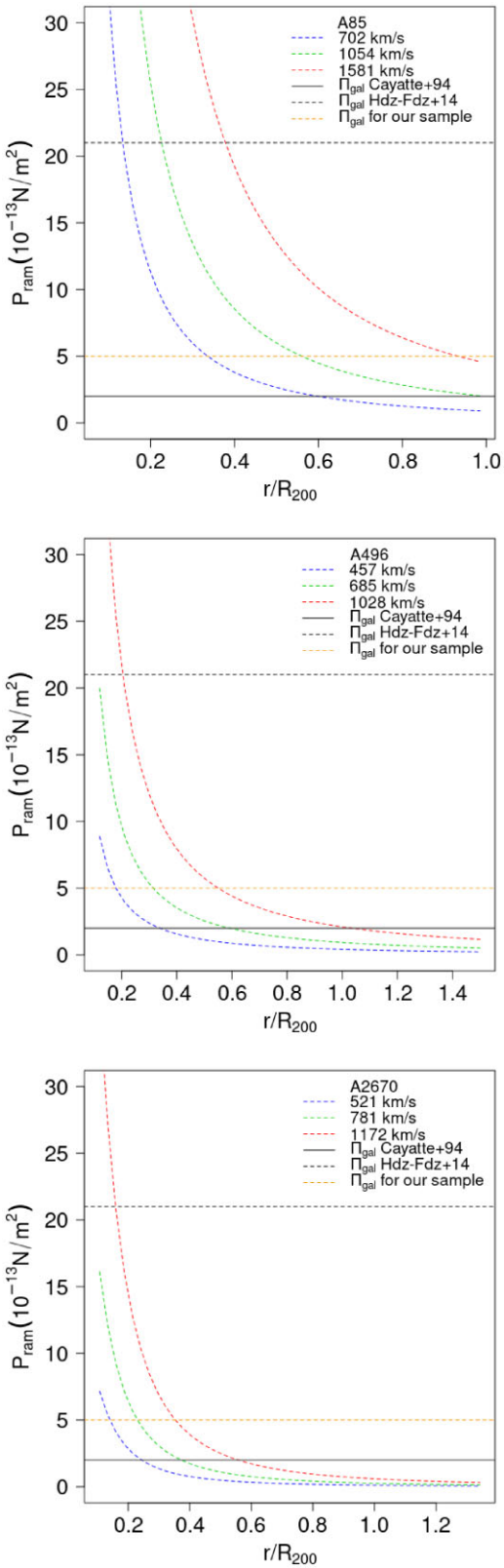

Figure 6. The RPS as a function of the cluster-centric distance. Three representative velocities relative to the ICM are displayed, taking the cluster velocity dispersion as a reference: $0.66\sigma_{\rm cl}$ in blue; $1.0\sigma_{\rm cl}$ in green, $1.5\sigma_{\rm cl}$ in red. Three values of the anchoring force are shown in order to evaluate the RPS effects (see text).

In order to quantify the effects produced by the RPS on individual objects, they must be compared with the anchoring force per unit surface produced by the galaxy gravitational potential, given by $\Pi_{gal} = 2\pi\, G\, \Sigma_{\rm s}\, \Sigma_{\rm g}$. Here, $\Sigma_{\rm s}$ and $\Sigma_{\rm g}$ are the surface densities of the stellar and gaseous discs, respectively. RPS must overcome the anchoring force in order to succeed the gas stripping. Several values of $\Pi_{\rm gal}$ have been proposed, going from 2.0×10^{-13} N m^{-2} for spirals in Virgo (Cayatte et al. 1994), to 2.1×10^{-12} N m^{-2} for a Milky Way-like galaxy (Hernández-Fernández et al. 2014). One step further was made by Jaffé et al. (2018) who modelled the anchoring force as a function of the galaxy radius, the stellar mass, and the gas fraction of a sample of spirals. We follow these authors in order to seek for values of $\Pi_{\rm gal}$ being representative for our sample of B-Sp.

From Fig. 2, we see that most of the B-Sp are in the range of mass between $\log(M_*/{\rm M}_\odot) = 9.0$ and $\log(M_*/{\rm M}_\odot) = 10.5$. No significant difference in mass is expected between our sample and that studied by Jaffé et al. (2018), so we use their Fig. 5 (and Fig. 4 in Jaffé et al. 2019), which provides the anchoring force at a radius of twice the disc scale length. As we are interested in the RPS effects exerted at the external edge of spirals, we take this value as a proxy for the anchoring force acting at the outskirts of the galaxy. This strategy delivers $\Pi_{\rm gal}$ in the range from 10^{-12} to 10^{-13} N m^{-2}. We take the middle value 5.0×10^{-13} N m^{-2} as a reference for our sample of B-Sp. As a comparison, the $\Pi_{\rm gal}$ value reported by Cayatte et al. (1994) predicts very strong RPS effects, even in the low-velocity and at large cluster-centric domains (see Fig. 6). The opposite is given by the value of $\Pi_{\rm gal}$ proposed by Hernández-Fernández et al. (2014). We indicate the three values of $\Pi_{\rm gal}$ in Fig. 6. It is clear that the reference value $\Pi_{\rm gal} = 5.0 \times 10^{-13}$ N m^{-2} is more realistic for the bright spirals under study, so we use it along the forthcoming analysis.

Some uncertainties are introduced though. Particularly important is the dispersion in the relation between the anchoring force and the stellar mass, with a strong dependence on the galaxy radius. In this respect Jaffé et al. (2018) have shown that the anchoring force is strongly dependent on the degree of mass concentration; this implies that low mass objects with a high central density could have a similar $\Pi_{\rm gal}$ at their centre than a more massive/extended galaxy at its edge. Despite these uncertainties we will show (Section 6) that our reference value of $\Pi_{\rm gal}$ matches reasonably well with our observations on a statistical basis.

We repeat this analysis for the low-mass galaxies, i.e. those in the range of stellar mass $\log(M_*/{\rm M}_\odot)$ between 8.0 and 9.0, obtaining an upper limit for the anchoring force of $\Pi_{\rm gal} = 10^{-13}$ N m^{-2}. Galaxies in this low regime of $\Pi_{\rm gal}$ are predicted to be easily stripped of their cold gas when they approach the virial radius. We further discuss about these objects in Section 6.

5.2 Phase-space diagrams and cluster accretion history

The projected phase-space (PPS) diagram of a cluster helps to distinguish virialized from infalling galaxies (*e.g.* Kent & Gunn 1982; Geller et al. 2013; Oman, Hudson & Behroozi 2013; Jaffé et al. 2015; Rhee et al. 2017; Cortese et al. 2021). We present a version of PPS where the parameters Δv and the radius are normalized by the velocity dispersion $\sigma_{\rm cl}$, and by R_{200}, respectively. On the *y*-axis we display the absolute value of the peculiar velocity ($|\Delta v_{\rm rad}|/\sigma_{\rm cl}$). On the *x*-axis the projected position relative to the cluster centre is normalized by R_{200}.

Fig. 7 shows the PPS diagrams for A85, A496, and A2670 with the same symbols as in previous figures. The escape velocity of each cluster is shown with a solid grey line; these are more conservative

Downloaded from https://academic.oup.com/mnras/article/517/1/1218/6694106 by CNRS user on 13 April 2023

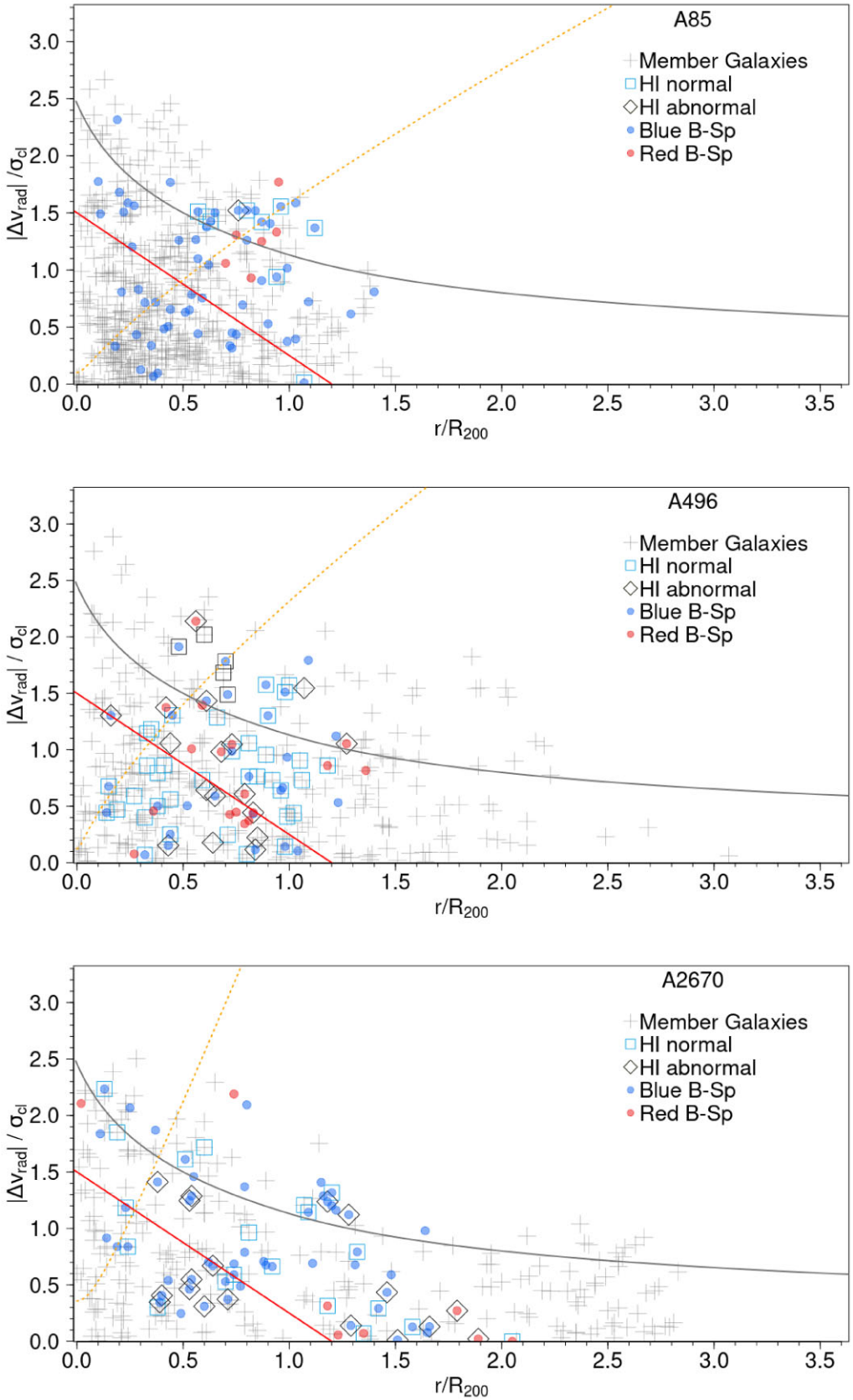

Figure 7. PPS diagrams for A85 (top panel), A496 (middle panel), and A2670 (bottom panel). Symbols are the same as in Figs 2 and 3. The solid red line defines the virialized region (see text) and the solid grey line indicates the escape velocity. The dotted orange line shows the region where $P_{\rm ram} = \Pi_{gal}$ (see Section 5.1).

Downloaded from https://academic.oup.com/mnras/article/517/1/1218/6694106 by CNRS user on 13 April 2023

than the caustics used to define the member sample and helps to obtain a better contrast between virialized and infalling galaxies (e.g. Jaffé et al. 2015; Wang et al. 2021). This escape velocity was estimated on the basis of a NFW halo with a concentration of $c = 6$; other values of this parameter do not change the escape velocity significantly. The orange dotted line draws the boundary where RPS equals the anchoring force, $\Pi_{\rm gal} = 5.0 \times 10^{-13}\,{\rm N\,m^{-2}}$.

At the lower left-hand corner of the PPS diagram, we find the galaxies projected at short cluster-centric distances and having low (radial) velocities relative to the cluster. These objects are likely settled on to the cluster potential after completing, at least, one pericentric passage. This part of the diagram is identified as the *virialized zone*, and we define its boundaries as follows. On the *x*-axis, we followed authors (e.g. Jaffé et al. 2015; Kopylova & Kopylov 2018) who propose that the virial radius lies in the range 1.2–1.4 R_{200}. On the *y*-axis, the criteria to define the virial zone are based on statistics, by considering a Gaussian distribution of velocities. We use the value of 1.5 σ as a more restrictive limit (compared with 3σ) in order to avoid contamination by foreground/background galaxies. Considering these boundaries, we define the virialized zone as the triangle limited by the solid red line in Fig. 7. This triangle zone is more conservative than the corresponding squared region and has been applied by authors like Jaffé et al. (2015) and Wang et al. (2021). On the opposite corner of the PPS diagrams, galaxies infalling for the first time lie in the large radii/velocity domain. After a few 10^9 yr, equivalent to the crossing time for a typical cluster, infalling galaxies will lose kinetic energy due to dynamical friction and violent relaxation, and they will settle deep into the cluster gravitational potential.

The distribution of different types of galaxies in the PPS diagrams offer important hints on the dynamical stage of the three clusters. The top panel of Fig. 7 shows A85 behaving as a typical evolved system with a high concentration of member galaxies within the virialized zone. The escape velocity curve in this plot is lower than the one reported by Bellhouse et al. (2017); this is due to the higher mass used for A85 by these authors $M_{200} = 1.58 \times 10^{15}\,{\rm M_\odot}$ We see a clear trend where, with one single exception, all B-Sp lying below the escape velocity curve are not detected in HI, suggesting that these galaxies have gone through an advanced process of gas stripping. The gas-rich objects in A85 lie in the high radius, high-velocity domain, indicating that they approach the cluster for the first time. Despite some similarities between A85 and other systems like A693 (e.g. mass, morphology, and dynamical stage), their distribution of galaxies across their PPS differs significantly (Jaffé et al. 2015).

Similar to A85, A496 harbours a crowded virialized zone (medium panel of Fig. 7). This is in agreement with the advanced level of relaxation reported by different authors and with the low degree of substructuring in A496 reported in this work (Section 4). The striking number of HI-rich galaxies lying within the virialized zone can be explained by projection effects as described in Section 3.2. The PPS diagram of A496 shows a slight trend of HI abnormal galaxies (black diamonds) and red spirals (red solid circles) being more abundant towards the virialized zone.

A2670 is dynamically young, accounting for the complex distribution of galaxies in the PPS diagram and a virialized zone significantly less concentrated than in the other two systems. In this respect, A2670 looks like other young clusters like Hydra (Wang et al. 2021). A number of HI detections are projected on to the virialized zone, certainly explained by projection effects. Other HI galaxies are located in the high radius ($\geq 1.5\,r/R_{200}$) domain, matching with the substructure reported on to the SW in Section 4. Several of these detections correspond to abnormal HI galaxies (black diamonds) and to red spirals, which are good candidates to be under pre-processing.

6 DISCUSSION

6.1 The HI and the effects of environment

The results described so far provide undeniable evidence on the important role played by environment in the transformation of spirals in the three studied clusters. The global cluster HI deficiency is an important parameter that correlates with the properties of galaxies in most of the nearby clusters. In this work, we approach the cluster deficiency as the ratio of high HI deficient B-Sp (i.e. those not detected in HI) normalized by the total number of B-Sp found within each system. Cluster deficiencies calculated in this way are: 0.86, 0.37, and 0.46, for A85, A496, and A2670, respectively. A85 appears as an extreme case of HI deficiency and, since it is the most massive of the three studied systems, this result matches the model prediction of more massive haloes producing larger gas loss (*e.g.* Donnari et al. 2021).

Next, we discuss our results in the frame of four milestone results and predictions on galaxy evolution in clusters, which are based on observations and on theoretical models: (1) The dependency of individual galaxy properties (like gas content and SF quenching) on the cluster-centric distance. (2) The commonly accepted role played by RPS in galaxy transformation, at least in the inner cluster regions. (3) The pre-processing of galaxies at large cluster-centric radii is thought to be responsible for the transformation of large fractions of galaxies. (4) Models of galaxy evolution predict the transformation (quenching and gas sweeping) of large fractions of satellite galaxies previous to their infalling (we refer to the following works and references therein, Peng et al. 2010; Rhee et al. 2017; Jung et al. 2018; Roberts et al. 2019; Cortese et al. 2021; Donnari et al. 2021; Healy et al. 2021; Boselli et al. 2022).

We explore how the three studied clusters fit within these predictions taking into account the results described in the previous sections. With this aim, we use our sample of B-Sp as test particles for environment effects. As a first approach, we consider that a normal HI content *plus* a blue colour constitute an indicator of a non-quenched galaxy. As mentioned previously, optical colours are not the most accurate tracers for quenching but they are often used as an alternative, distinguishing active from non-active galaxies, for instance in statistical studies as the present one. In the following discussion, we take our sample of B-Sp as analogues of the *satellite* galaxies defined in cosmological simulations. We observe that none of the B-Sp dominates any of the groups reported in Section 4, giving support to this approach. Current models (*e.g.* Xie et al. 2020) predict that evolution of low mass galaxies, those having $\log(M_*/{\rm M_\odot}) < 10.3$ (matching the range of our B-Sp) is dominated by environmental effects. Above this threshold AGN feedback is expected to drive the galaxy quenching.

6.2 Global properties of the studied clusters

Here, we compare some physical properties of the studied clusters with each other. In order to avoid part of the observational bias we focus on the inner regions, more specifically on the largest physical radius being observed with the VLA in the three systems. Based on this criteria, we take the conservative value of 1 R_{200} as comparison radius. Obviously, some bias remain due to different cluster distances, which has an effect on the population of HI detected galaxies. For instance, typical HI masses reported in A85 and A2670

Downloaded from https://academic.oup.com/mnras/article/517/1/1218/6694106 by CNRS user on 13 April 2023

Table 6. Different types of galaxies within 1 R_{200}: comparing the inner regions of A85, A496, and A2670.

Galaxies	Normalized by:	A85 #	A85 (fract.)	A496 #	A496 (fract.)	A2670 #	A2670 (fract.)
(1)	(2)	(3)	(4)	(5)	(6)	(7)	(8)
Members		574		271		195	
HI-det	Members	8	0.01	52	0.19	21	0.11
B-Sp	Members	58	0.10	39	0.14	35	0.18
B-Sp HI-det	B-Sp	7	0.12	27	0.69	17	0.49
B-Sp HI non-det	B-Sp	51	0.88	12	0.31	18	0.51
B-Sp in red seq	B-Sp	6	0.10	14	0.36	2	0.06
HI-det in red seq	HI-det	0	0.00	7	0.13	0	0.00
HI-det abnormal	HI-det	1	0.13	15	0.29	10	0.48
Low-mass HI-det	HI-det	1	0.13	21	0.40	3	0.14

Notes:
– All objects mentioned in Columns 1 and 2 are restricted to 1 R_{200}.
– The numbers of galaxies mentioned in Column 1 are given in columns 3 (A85), 5 (A496), and 7 (A2670).
– Column 2 indicates the sample used to normalize the number of galaxies referred in Column 1.
– The fractions *'Column (1) / Column (2)'* are given in Columns 4 (A85), 6 (A496), and 8 (A2670).

approach 8×10^9 M$_\odot$, while in A496 this value is $\sim 2 \times 10^9$ M$_\odot$. As a consequence, in this last cluster, we report more HI galaxies in the low mass regime (Section 3). Nonetheless, some peculiarities described below remain even after considering this observational bias. Table 6 resumes the data corresponding to 1 R_{200} for the three clusters.

6.2.1 A85

This stands out as a very HI-deficient system. The HI detections represent a fraction of 0.016 of the member galaxies within 1 R$_{200}$ (Table 6). The majority of the B-Sp not detected in HI (Fig. 7) gather towards the virial zone of the PPS diagram. This cluster shows the expected cluster-centric distribution of gas-rich/gas-poor spirals. The strongest ICM effects in A85, compared with A496 and A2670, are supported by two results given in Table 6 within 1 R_{200}: (a) the low fraction of HI detected galaxies relative to the member objects (0.01, 0.19, and 0.11, in A85, A496, and A2670, respectively); and (b) the fraction of B-Sp not detected in HI, relative to the B-Sp reported within the same region (0.88, 0.31, and 0.51, in A85, A496, and A2670, respectively). These numbers do not correlate with redshift so we discard any observational bias as responsible for this result.

These effects are well explained by RPS. We showed (Section 5.1) that this mechanism might exceed the anchoring force up to a radius close to 0.6 r/R_{200} for typical (1σ) velocities, and up to 0.9 r/R_{200} for faster infallers (1.5σ; see Fig. 6). As a matter of fact, the central regions of A85 could be an extreme case even compared with Coma, where a number of gas-deficient spirals are still detected within 1 Mpc, with similar HI mass limit detection than the present work (Bravo-Alfaro et al. 2000; Healy et al. 2021; Molnár et al. 2022). In A85, the only HI projected close to the centre is the high-speed infalling jellyfish JO201, which shows signs of strong ram pressure stripping (Ramatsoku et al. 2020; Luber et al. 2022).

In parallel to RPS, we inspect the role played by pre-processing and by the shocked interface between A85 and the SE-group, in the transformation of infalling spirals. A large majority of the B-Sp, which are not detected in HI are located in the SE quadrant, where the shocked interface is found. The complexity of this region is consistent with the presence of two groups (the South Blob and the Filament groups) in addition to the SE subcluster itself (Fig. 5). Another jellyfish galaxy (JO200) is located in this zone being so deeply stripped that it was not detected in HI down to a mass limit of 9×10^8 M$_\odot$ (A85[DFL98]286 in Table B1). Venkatapathy et al. (2017) already proposed this galaxy to be in a more advanced stage of transformation than JO201.

A remaining number of HI non-detected B-Sp galaxies lies in the NW quadrant of A85 (Fig. 3). These objects are seen slightly beyond the escape velocity curve of the PPS in Fig. 7. No substructures are reported in that zone; therefore we favour the backsplash hypothesis (Gill, Knebe & Gibson 2005; Hirschmann et al. 2014). This suggests that these galaxies had entered A85 from the SE and now we see them projected to the NW. Timescales for RPS quenching ($\sim$1 Gyr) and for cluster crossing ($\sim$3 Gyr) are in good agreement. Considering that morphology transformation, disregarding the responsible mechanism, takes longer timescales ($\sim$10 Gyr), backsplash is a plausible explanation for the spiral morphology and their location within the cluster (Boselli & Gavazzi 2006, 2014; Cortese et al. 2021).

As a first approach to quantify pre-processing in A85, we obtained the number of HI perturbed galaxies, and those non-detected, within each of the groups reported in Section 4. We obtained the following numbers: SB:3, Filament: 4, SE: 4, SW: 0, NE: 1. This suggests that pre-processing could be at work within the groups located SE of A85. However, it is difficult to separate pre-processing from the effects of the interface shocking region. The later covers very well the zone where the B-Sp not detected in HI are found.

The sample of blue, HI normal galaxies in A85 projected between 1.5 and 3.0 Mpc east of the cluster centre raises some unanswered questions. They are confirmed as cluster members and, being in the stellar mass range log(M_*/M$_\odot$) between 9.0 and 10.0, these objects are predicted to have a high probability to be quenched before their complete infall on to a massive cluster like A85 (e.g. Bahé et al. 2019). For instance, Xie et al. (2020) estimates that $\sim$60 per cent of galaxies would be quenched in the mass range given above and haloes (clusters) with masses above log($M_{\rm halo}$/M$_\odot$) = 14.0, which is the case for this cluster.

In any case, the gas-rich galaxies in A85 seem to be part of a continuous flow of newcomers occurring during several Gyr. This scenario is supported by the fact that A85 is part of the supercluster MSCC-039, which includes eleven systems (Chow-Martínez et al. 2014). The large scale structure joining A85 with its neighbours, in particular A117A, projected at $\sim$12 Mpc SE of A85 (Caretta, private communication), could be responsible for the feeding of fresh HI galaxies and with the presence of the SE subcluster.

Downloaded from https://academic.oup.com/mnras/article/517/1/1218/6694106 by CNRS user on 13 April 2023

6.2.2 A496

This cluster constitutes a puzzle not only compared with the two other systems under study but also relative to the low-z clusters previously imaged in HI. On one hand A496 is confirmed as a relaxed system and, in agreement with this, it is very concentrated. The PPS of Fig. 7 shows that more than 50 per cent of member galaxies lie within the virialized zone. However, A496 presents some features in apparent contradiction with an evolved system. First, the high number of HI detections (58) constitutes 17 per cent of the member galaxies within the VLA FoV (this is below 2 per cent in A85; see Table 4). Even if we compensate for A496 being closer than the other two systems the trend clearly persists. Another paradox is the absence of the expected cluster-centric distribution of HI galaxies. This is observed in clusters like Coma and A85, comparable to A496 in dynamical stage. Figs 3 and 4 clearly show the lack of correlation. As mentioned before, particularly strong projection effects should explain the HI-rich galaxies projected on to the cluster core. This scenario fits with active ram-pressure stripping in this cluster. Our estimations predict that RPS surpass the anchoring force at $\sim$0.4 r/R_{200} for typical 1σ velocities, and up to 0.6 r/R_{200} for velocities of 1.5σ (Fig. 6). This implies that HI normal spirals are hardly expected near the cluster core.

Taking the full sample of B-Sp as test particles for environment effects we find that 37 per cent of them have lost a large fraction of gas and were not detected in HI (Table 4). Furthermore, among the HI detected B-Sp a number of them are reported as abnormal (Table A2). If we consider the colour index, one third of the B-Sp in A496 are located in the red sequence. All these results clearly indicate an important degree of spiral transformation in this cluster.

Another intriguing result in A496 is the large number of HI detected galaxies with masses below $\log(M_*/\mathrm{M}_\odot) = 9.0$, some of them having HI mass $\geq 3 \times 10^9\,\mathrm{M}_\odot$ (see Table A2). In similar clusters, like Hydra, the average HI mass for the same range of stellar mass is significantly lower, below $10^9\,\mathrm{M}_\odot$ (Wang et al. 2021). Even considering the closer distance of A496 (the nearer the cluster, larger the fraction of low-mass HI detected objects), we expected similar galaxies to be found in A85 and A2670. Taking into account our HI detection limits and by scaling the corresponding HI flux to the distance of A85 and A2670, our survey would be capable to detect such gas-rich galaxies with stellar masses around $\log(M_*/\mathrm{M}_\odot) = 8.5$. However these objects are absent, more conspicuously in A85.

The low-mass, gas-rich, and very blue galaxies in A496, are very likely in a pre-quenching phase. These objects deserve a more detailed study; current models predict strong pre-processing and a significant quenching fraction, going up to 80 per cent for $\log(M_*/\mathrm{M}_\odot) = 9.0$, at $z = 0$ (Donnari et al. 2021). In a forthcoming paper we will try to determine, statistically, how close to a massive halo these low-mass galaxies last before extinguishing. This could help to restrict theoretical models.

Besides the projection effects, the full distribution of HI galaxies in A496 (Fig. 3) deserves a closer look. The NE quadrant is almost empty of HI objects. In the south and south-east regions, all the HI detections belong to the high-velocity domain (red maps in Fig. 4), suggesting a common origin. Finally the north-west is the richest zone of both, HI detections and member galaxies. This could be associated with the only substructure found in this cluster (Section 4). Concerning pre-processing, the very low degree of substructures suggests that this mechanism is not playing a major role transforming infalling galaxies in A496. Instead, the cluster environment seems to dominate the processing of spirals.

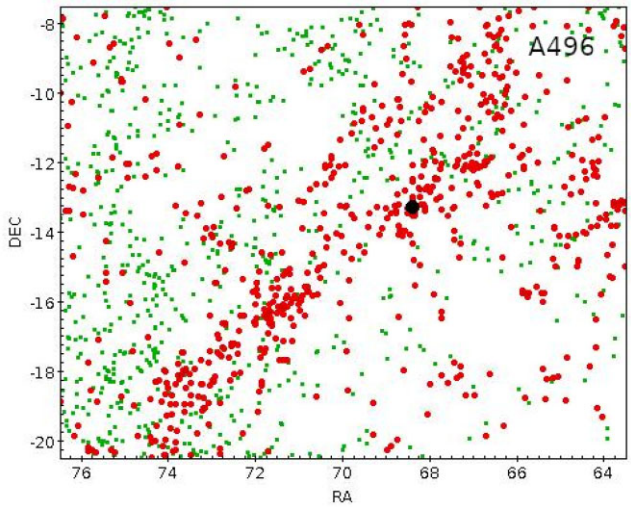

Figure 8. 6dF galaxies (green dots) found within a *square* of 12° of side around A496 (black diamond). Red dots indicate the 498 galaxies having velocities within the 3σ interval around A496.

We explored the surrounding large-scale structure of A496 in order to better understand the replenishment of gas-rich galaxies. We analysed 6dF Survey data within an area of 12° around A496; the centre of this cluster is indicated with a black solid circle in Fig. 8. We applied a galaxy request restricted to the redshift range of 0.0255–0.0407 (7552–11962 km s^{-1}), corresponding to the 3σ interval of A496. The output of 498 galaxies is displayed in the same figure. This plot shows in green the positions of all the galaxies found in 6dF, while the objects in red correspond to the selected redshift interval. Important galaxy concentrations are clearly seen, drawing a filament in the NW-SE direction, having redshifts of 0.037 and 0.038 (the redshift of A496 is 0.033). The nearest structure to A496 lies to the NW and could be at the origin of the large number of gas-rich objects in the NW zone of A496 and the substructure reported in the same region (Fig. 5). Other observational pieces of evidence support this filament of large scale structure, like the X-ray cluster MCXC J0445.1−1551, SE from A496. This system was not identified originally by Abell and is found at RA=71.5, Dec. = −16, centred on the cD galaxy NGC 1650. These filaments account for the observed replenishment of gas-rich galaxies, in particular from the NW.

6.2.3 A2670

This system is dynamically younger than the other studied clusters so the high fraction of B-Sp within the VLA FoV (24 per cent, see Table 4) is not unexpected. The fraction of B-Sp within 1 R_{200} is larger than in the other two systems (Table 6). However, opposite to other young clusters like Virgo (Chung et al. 2009), Hydra (Wang et al. 2021), and Abell 963 (Jaffé et al. 2015), the correlation between HI deficiency and cluster-centric radius is not seen in A2670. This is due to the large number of HI-rich galaxies projected on to the cluster core (Figs 3 and 4), which are located into the virialized zone of the cluster (Fig. 7). Our estimations of RPS in A2670 predict significant environment effects, even if less intense than in A496 and A85. In A2670, RPS is expected to dominate within $r/R_{200} \leq 0.3$, for relative velocities of $\sim$1.0σ, and within a radius of $r/R_{200} \leq 0.4$, for higher velocities $\sim$1.5σ (Fig. 6,). Therefore, most of the HI detections projected in the very central region of A2670 are explained by projection effects,

Downloaded from https://academic.oup.com/mnras/article/517/1/1218/6694106 by CNRS user on 13 April 2023

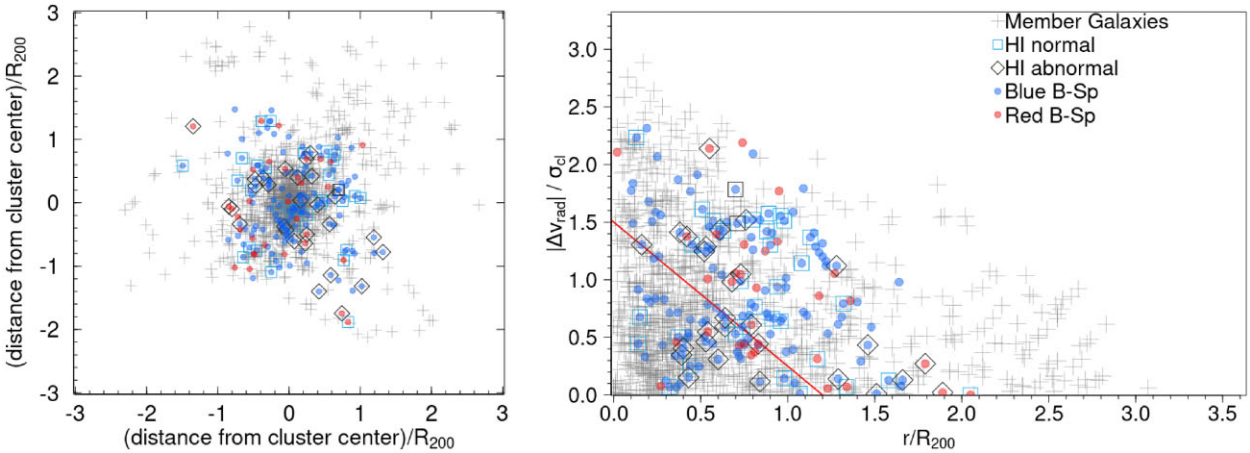

Figure 9. Composite plots of three clusters showing the member galaxies (grey crosses), highlighting the bright spirals; blue/red spirals are shown with solid circles; HI detections are given with squares and diamonds, indicating normal and abnormal objects, respectively. left-hand panel: the projected position on the sky, normalizing cluster-centric distances by R_{200}. Right-hand panel: positions of galaxies in the phase space diagram. The red line delimits the virialized zone as defined in Fig. 7.

either being fast infallers along the line of sight or objects with non-radial orbits.

We use the B-Sp properties to investigate the strength of the environment effects in A2670. Fig. 2 shows that a number of B-Sp have reached the red sequence; five of them retain enough gas to be detected in HI. Interestingly, almost half of the HI detected galaxies are classified as abnormal (Table 4), confirming a rather harsh cluster environment. The fraction of HI abnormal objects within $1\,R_{200}$ is much larger in A2670 (0.48) than in the other two clusters. We quantify the importance of pre-processing in A2670 by contrasting the positions of the HI perturbed B-Sp with the substructures reported in Section 4. We found only two of such galaxies in the north-centre (NC) group and four in the SW, including 3 HI abnormal and one non-detected object. The SW region seems to be the only zone of this cluster where pre-processing is at work.

The elongated morphology of A2670, following a NE-SW axis, is confirmed by the distribution of member galaxies in Fig. 3. The global positions of HI detections help to trace the accretion history of A2670. When we focus beyond $1.0\,R_{200}$, a strong asymmetry is seen between the very HI-rich south-west and the HI-poor north-east region (Fig. 4). This strongly suggests the former as the preferred direction of infalling spiral galaxies.

6.3 The evolutionary stage of the bright spirals: a three-cluster composite view

In order to explore the global behaviour of the large sample of bright spirals (B-Sp) collected in this work, we create a composite cluster constituted by the three studied systems. The left-hand panel of Fig. 9 shows the distribution, on the plane of the sky, of all member objects and all the bright spirals (we use the same symbols as in previous plots). The right-hand panel of Fig. 9 shows the PPS diagram of the composite cluster. In order to properly display the three systems in a single plot, we normalize the galaxy cluster-centric distance by the corresponding R_{200}. The relative velocities are normalized by the corresponding cluster velocity dispersion $\sigma_{\rm cl}$ (see Luber et al. 2022).

We study the behaviour of the B-Sp across the composite cluster by looking for trends between their distribution and their HI properties. We split the full catalogue of B-Sp in two sub-samples named: *normal* B-Sp and *disturbed* B-Sp. The former is constituted by those HI detected B-Sp, displaying normal distribution and gas content. The sub-sample of *disturbed* B-Sp includes those being HI abnormal *plus* those HI non-detected. Defined in this way, the disturbed sub-sample includes galaxies undergoing strong degrees of transformation. Next, we estimate the mean projected distances for each sub-sample and we compare them. We use units of r/R_{200}, obtaining the following results:

normal B-Sp: $\mu_1 = 0.63$;

disturbed B-Sp: $\mu_2 = 0.56$.

This confirms the expected scenario where HI disturbed spirals are located, on average, closer to the cluster centre than HI normal ones. The difference between means is, however, not found to be significant enough ($1 - p \lesssim 90$ per cent) by the Welch's t-test. As we next show, this is most likely due to the heterogeneous trends seen in the individual clusters. In order to quantify such trends, we contrasted the average distances of the same sub-samples within each system:

A85: normal B-Sp: $\mu_1 = 0.86$ versus disturbed B-Sp: $\mu_2 = 0.59$.

A496: normal B-Sp: $\mu_1 = 0.66$ versus disturbed B-Sp: $\mu_2 = 0.75$.

A2670: normal B-Sp: $\mu_1 = 0.96$ versus disturbed B-Sp: $\mu_2 = 0.85$

This confirms, in A85, the very strong trend where disturbed B-Sp lay at lower cluster-centric radius (confidence value > 99 per cent). Oppositely, A496 has a very atypical behaviour with an inverse trend of normal B-Sp located, in average, at lower radius than their disturbed counterparts. Despite the projection effects cited above, such a trend has never been observed in other clusters. A2670 is an intermediate case where the difference between μ_1 and μ_2 has low statistical significance. Other statistical methods produce similar results, for instance, the two-sample test for the mean, considering the one-tail case of the z-Test.

Downloaded from https://academic.oup.com/mnras/article/517/1/1218/6694106 by CNRS user on 13 April 2023

7 SUMMARY AND CONCLUSIONS

This paper is devoted to study galaxy evolution and environment effects occurring at the core and outskirts of three nearby Abell clusters: A85/A496/A2670. We analysed the transformation of spirals as a function of their local environment by studying different clusters lying at roughly the same cosmological epoch. This work is based on a blind, VLA HI-imaging survey, with data cubes covering a volume that extends beyond one virial radius and more than three times the velocity dispersion of each cluster. Our main results and conclusions can be summarized as follows:

(i) We report HI parameters for 10, 58, and 38 galaxies in A85, A496, and A2670, respectively, as well as an atlas of the corresponding HI maps and velocity fields. We defined a complete sample of bright spirals with masses above $\log(M_*/\mathrm{M}_\odot) = 9.0$ and we used them as test particles for environment effects. This sample helped as well to obtain a catalogue of the spirals not detected in HI and to trace the accretion history of the parent clusters.

(ii) We report further evidence for cluster environment playing an active role in transforming spirals, both in their HI content and in their colour. We measured the global HI deficiency of the three clusters, finding a very high value (85 per cent) for A85, and less conspicuous deficiencies for A496 and A2670. The expected cluster-centric distribution of HI-rich/poor galaxies is only observed in A85. The other two systems show a very complex distribution of their HI, with a high fraction of gas-rich objects lying within the virialized zone. Strong projection effects must be responsible.

(iii) We report a number of bright spirals that have moved into the red sequence in the three clusters. The majority of these objects are HI disturbed. This sample of red spirals constitutes additional evidence for systematic transformation from normal, blue spirals, into gas-poor, passive objects.

(iv) We traced ram-pressure stripping profiles in order to measure the strength of environment effects due to the intracluster medium. We find that RPS accounts for the disrupted/stripped galaxies in the central regions of the three studied clusters. The inner 1.5 Mpc (roughly one virial radius) of A85 appears to be particularly harsh, only compared with clusters like Coma.

(v) Our substructure analysis confirms A85 as a complex system with several minor groups and a major SE subcluster merging with the main cluster body. We report two new groups in A85, one to the SW and a second to the NE. In A496 we unveiled a large group NW of the cluster centre. We revisited the surrounding large-scale structure of A496 and we detected a filament running NW-SE. A2670 is an intermediate case between the two other studied clusters, having three minor groups running along the NE-SW axis. The distributions of HI-rich/poor galaxies in the three clusters reveal the following (preferred) directions of galaxy infalling: the SE for A85, NW for A496, and SW for A2670.

(vi) We explored the relevance of pre-processing by measuring the number of HI disturbed galaxies within each of the reported substructures. In A85 we found an important number of such disturbed objects, SE from the cluster centre. They could be produced by a shocked interface due to a cluster-subcluster merger process and/or by pre-processing. The other two clusters show no evidence for strong pre-processing with the exception of the SW group of A2670. Our results suggest that the effects of the global cluster environment are equally (or even more) important than pre-processing in the transformation of spiral galaxies.

(vii) The systematic transformation of spirals in the studied clusters cannot be associated to one single parameter of the parent system. Therefore, in addition to the cluster mass and L_X, the dynamical stage and the feeding of new spirals from the large scale structure help to explain the observed properties of the spiral population and their degree of transformation.

ACKNOWLEDGEMENTS

We thank the NRAO for generous allocation of observing time and the VLA staff for their support with data reduction. The authors thank the anonymous referee for her/his helpful comments, which helped to improve this paper. MMLG, HBA, and CAC acknowledge funding from CONACyT and DAIP. H.B.A. also thanks the *Institut d'Astrophysique de Paris* for its support during his working visits. We acknowledge Y. Venkatapathy for his help in enlarging the redshift catalogues used in this work. FD acknowledges continuous support from CNES since 2002. YJ acknowledges financial support from FONDECYT Iniciación 2018 No. 11180558 and ANID BASAL Project FB210003.

DATA AVAILABILITY

Data available on request.

REFERENCES

Arnouts S. et al., 2007, A&A, 476, 137
Bahé Y. M., McCarthy I. G., Balogh M. L., Font A. S., 2013, MNRAS, 430, 3017
Bahé Y. M. et al., 2019, MNRAS, 485, 2287
Balogh M. et al., 2004, MNRAS, 348, 1355
Barnes J. E., Hernquist L., 1996, ApJ, 471, 115
Barsanti S. et al., 2018, ApJ, 857, 71
Barway S., Kembhavi A., Wadadekar Y., Ravikumar C. D., Mayya Y. D., 2007, ApJ, 661, L37
Bellhouse C. et al., 2017, ApJ, 844, 49
Boselli A., Gavazzi G., 2006, PASP, 118, 517
Boselli A., Gavazzi G., 2014, A&ARv, 22, 74
Boselli A. et al., 2021, A&A, 646, A139
Boselli A., Fossati M., Sun M., 2022, A&ARv, 30, 3
Boué G., Adami C., Durret F., Mamon G. A., Cayatte V., 2008a, A&A, 479, 335
Boué G., Durret F., Adami C., Mamon G. A., Ilbert O., Cayatte V., 2008b, A&A, 489, 11
Bravo-Alfaro H., Cayatte V., van Gorkom J. H., Balkowski C., 2000, AJ, 119, 580
Bravo-Alfaro H., Cayatte V., van Gorkom J. H., Balkowski C., 2001, A&A, 379, 347
Bravo-Alfaro H., Caretta C. A., Lobo C., Durret F., Scott T., 2009, A&A, 495, 379
Briggs D. S., 1995, BAAS, 27, 1444
Butcher H., Oemler A., 1978, ApJ, 219, 18
Byrd G., Valtonen M., 1990, ApJ, 350, 89
Cavaliere A., Fusco-Femiano R., 1976, A&A, 49, 137
Cayatte V., van Gorkom J. H., Balkowski C., Kotanyi C., 1990, AJ, 100, 604
Cayatte V., Kotanyi C., Balkowski C., van Gorkom J. H., 1994, AJ, 107, 1003
Chen Y. et al., 2007, A&A, 466, 805
Chow-Martínez M., 2019, PhD Thesis, Univ. Guanajuato, Mexico
Chow-Martínez M., Andernach H., Caretta C. A., Trejo-Alonso J. J., 2014, MNRAS, 445, 4073
Chung A., van Gorkom J. H., Kenney J. D. P., Crowl H., Vollmer B., 2009, AJ, 138, 1741
Cirimele G., Nesci R., Trèvese D., 1997, ApJ, 475, 11
Cortese L., Catinella B., Smith R., 2021, PASA, 38, 35
De Lucia G., Hirschmann M., Fontanot F., 2019, MNRAS, 482, 5041
Dénes H., Kilborn V. A., Koribalski B. S., 2014, MNRAS, 444, 667
Donnari M. et al., 2021, MNRAS, 500, 4004

Downloaded from https://academic.oup.com/mnras/article/517/1/1218/6694106 by CNRS user on 13 April 2023

Dressler A., 1980, ApJ, 236, 351
Dressler A., 1986, ApJ, 301, 35
Dressler A., Shectman S. A., 1988, AJ, 95, 985
Dressler A. et al., 1997, ApJ, 490, 577
Durret F., Forman W., Gerbal D., Jones C., Vikhlinin A., 1998, A&A, 335, 41
Durret F., Felenbok P., Lobo C., Slezak E., 1999, A&AS, 139, 525
Durret F., Adami C., Gerbal D., Pislar V., 2000, A&A, 356, 815
Durret F., Lima Neto G. B., Forman W., 2005, A&A, 432, 809
Fadda D., Biviano A., Marleau F. R., Storrie-Lombardi L. J., Durret F., 2008, ApJ, 672, L9
Fasano G., Poggianti B. M., Couch W. J., Bettoni D., Kjærgaard P., Moles M., 2000, ApJ, 542, 673
Fernández X. et al., 2013, ApJ, 770, L29
Fernández X. et al., 2016, ApJ, 824, L1
Finn R. A. et al., 2005, ApJ, 630, 206
Flewelling H. A. et al., 2020, ApJS, 251, 7
Geller M. J., Diaferio A., Rines K. J., Serra A. L., 2013, ApJ, 764, 58
Gill S. P. D., Knebe A., Gibson B. K., 2005, MNRAS, 356, 1327
Giovanelli R., Haynes M. P., 1985, ApJ, 292, 404
Giovanelli R. et al., 2005, AJ, 130, 2598
Gogate A. R. et al., 2020, MNRAS, 496, 3531
Goto T. et al., 2003, MNRAS, 346, 601
Gunn J. E., Gott J. R., 1972, ApJ, 176, 1
Haynes M. P., Giovanelli R., 1984, AJ, 89, 758
Haynes M. P. et al., 2018, ApJ, 861, 49
Healy J. et al., 2021, A&A, 650, A76
Hernández-Fernández J. D. 2014, MNRAS, 438, 2186
Hess K. M. et al., 2019, MNRAS, 484, 2234
Hirschmann M., De Lucia G., Wilman D. et al., 2014, MNRAS, 444, 2938
Ichinohe Y. et al., 2015, MNRAS, 448, 2971
Jaffé Y. L., Poggianti B. M., Verheijen M. A. W., Deshev B. Z., van Gorkom J. H., 2013, MNRAS, 431, 2111
Jaffé Y. L., Smith R., Candlish G. N., Poggianti B. M., Sheen Y.-K., Verheijen M. A. W., 2015, MNRAS, 448, 1715
Jaffé Y. L. et al., 2016, MNRAS, 461, 1202
Jaffé Y. L. et al., 2018, MNRAS, 476, 4753
Jaffé Y. L. et al., 2019, MNRAS, 482, 3454
Jonas J., MeerKAT Team, 2016, Proc. Sci., MeerKAT Science: On the Pathway to the SKA (MeerKAT2016). SISSA, Trieste, PoS#001
Jung S. L., Choi H., Wong O. I., Kimm T., Chung A., Yi S. K., 2018, ApJ, 865, 156
Kauffmann G. et al., 2004, MNRAS, 353, 713
Kent S. M., Gunn J. E., 1982, AJ, 87, 945
Kopylova F. G., Kopylov A. I., 2018, AstBu, 73, 267
Koribalski B. S. et al., 2020, Ap&SS, 365, 118
Laganá T. F., Durret F., Lopes P. A. A., 2019, MNRAS, 484, 2807
Larson R. B., Tinsley B. M., Caldwell C. N., 1980, ApJ, 237, 692
Lewis I. et al., 2002, MNRAS, 334, 673
Lopes P. A. A., Trevisan M., Laganá T. F., Durret F., Ribeiro A. L. B., Rembold S. B., 2018, MNRAS, 478, 5473
Luber N., Müller A., van Gorkom J. H. et al., 2022, ApJ, 927, 39
Mahajan S. et al., 2018, MNRAS, 475, 788
Masters K. L. et al., 2010, MNRAS, 405, 783
Merritt D., 1983, ApJ, 264, 24
Molnár D. Cs. et al., 2022, A&A, 659, A94
Moore B., Katz N., Lake G., 1996, ApJ, 457, 455
Nulsen P. E. J., 1982, MNRAS, 198, 1007
Oemler A., 1974, ApJ, 194, 1
Oman K. A., Hudson M. J., Behroozi P. S., 2013, MNRAS, 431, 2307
Paccagnella A. et al., 2017, ApJ, 838, 148
Paturel G., Fouque P., Bottinelli L., Gouguenheim L., 1989, A&AS, 80, 299
Peng Y.-J. et al., 2010, ApJ, 721, 193
Poggianti B. M. et al., 2009a, ApJ, 693, 112
Poggianti B. M. et al., 2009b, ApJ, 697, L137
Poggianti B. M. et al., 2017, ApJ, 844, 48
Postman M., Geller M. J., 1984, ApJ, 281, 95
Ramatsoku M. et al., 2020, A&A, 640, A22
Rhee J., Smith R., Choi H., Yi S. K., Jaffé Y., Candlish G., Sánchez-Jánssen R., 2017, ApJ, 843, 128
Rhee J., Smith R., Choi H., Contini E., Jung S. L., Han S., Yin S. K., 2020, ApJS, 247, 45
Roberts I. D., Parker L. C., Brown T., Joshi G. D., Hlavacek-Larrondo J., Wadsley J., 2019, ApJ, 873, 42
Salerno J. M. et al., 2020, MNRAS, 493, 4950
Scott T. C. et al., 2010, MNRAS, 403, 1175
Scott T. C., Brinks E., Cortese L., Boselli A., Bravo-Alfaro H., 2018, MNRAS, 475, 4648
Serna A., Gerbal D., 1996, A&A, 309, 65
Serra A. L., Diaferio A., Murante G., Borgani S., 2011, MNRAS, 412, 800
Sheen Y.-K. et al., 2017, ApJ, 840, L7
Slezak E., Durret F., Guibert J., Lobo C., 1998, A&AS, 128, 67
Slezak E., Durret F., Guibert J., Lobo C., 1999, A&AS, 139, 559
Solanes J. M. et al., 2001, ApJ, 548, 97
Spérone-Longin D. et al., 2021, A&A, 647, A156
Taylor G. B., Carilli C. L., Perley R. A., eds, 1999, ASP Conf. Ser. Vol. 180, Synthesis Imaging in Radio Astronomy II, A Collection of Lectures from the Sixth NRAO/NMIMT Synthesis Imaging Summer School. Astron. Soc. Pac., San Francisco
Tonnesen S., 2019, ApJ, 874, 161
Ulmer M. P., Adami C., Durret F., Ilbert O., Guennou L., 2011, A&A, 528, A36
Venkatapathy Y. et al., 2017, AJ, 154, 227
Vollmer B. et al., 2012, A&A, 537, A143
Walker I. R., Mihos J. C., Hernquist L., 1996, ApJ, 460, 121
Wang J. et al., 2021, ApJ, 915, 70
Xie L., De Lucia G., Hirschmann M., Fontanot F., 2020, MNRAS, 498, 4327
Bertin E., Arnouts S. 1996, A&A, 117, 393

SUPPORTING INFORMATION

Supplementary data are available at *MNRAS* online.

Figure S1: The H I-maps and velocity fields of detected galaxies in A85.
Figure S2: The H I-maps and velocity fields of detected galaxies in A496.
Figure S3: The H I-maps and velocity fields of detected galaxies in A2670.
Table S1: Catalogue of bright spirals (B-Sp) not detected in H I in Abell 85.
Table S3: Catalogue of bright spirals (B-Sp) not detected in H I in Abell 496.
Table S3: Catalogue of bright spirals (B-Sp) not detected in H I in Abell 2670.

Please note: Oxford University Press is not responsible for the content or functionality of any supporting materials supplied by the authors. Any queries (other than missing material) should be directed to the corresponding author for the article.

APPENDIX A: HI DETECTED GALAXIES IN A85, A496, AND A2670

Downloaded from https://academic.oup.com/mnras/article/517/1/1218/6694106 by CNRS user on 13 April 2023

Table A1. The HI detected galaxies in Abell 85.

ID	Name	RA (2000)	Dec (2000)	Morph. type	g mag	colour $(g-r)$	M_*	Opt-vel $km\,s^{-1}$	HI-vel $km\,s^{-1}$	Δv $km\,s^{-1}$	M_{HI} $10^9\,M_\odot$	Def_{HI} Sa-Sb	Def_{HI} Sc-Irr	Dist. Mpc	HI pert.
(1)	(2)	(3)	(4)	(5)	(6)	(7)	(8)	(9)	(10)	(11)	(12)	(13)	(14)	(15)	(16)
1	323	00 42 18.7	−09 54 14	S?*	17.86	0.376	9.50	15618	15608	137	8.2	−0.27	−0.13	2.39	*N*
2	347	00 42 29.5	−10 01 07	S?*	17.62	0.352	9.59	15165	15175	91	2.5	−0.03	0.08	2.86	*N*
3	374	00 42 41.5	−08 56 49	S?*	16.39	0.512	10.26	15106	15107	318	13.8	−0.29	−0.14	1.60	*N*
4	986362[b]	00 43 01.7	−09 47 34	–	17.27	0.418	9.79	15110	15107	227	6.5	−0.39	−0.27	2.23	*N*
5	461	00 43 14.3	−09 10 21	–	18.84	0.318	9.01	15015	15016	227	10.2	−0.85	−0.76	1.44	*N*
6	3114[a]	00 43 19.5	−09 09 13	–	19.47	0.390	8.76	15060	15061	136	3.7	−0.46	−0.37	1.54	*N*
7	486	00 43 31.2	−09 51 48	S	16.81	0.288	9.82	16619	16615	230	7.2	−0.09	0.05	2.72	*N*
8	491	00 43 34.0	−08 50 37	S?*	17.05	0.297	9.94	14968	14993	182	11.6	−0.56	−0.44	2.43	*N*
9	496	00 43 38.7	−09 31 21	S?*	16.99	0.281	9.84	15004	14993	182	4.3	0.04	0.17	1.94	*Pos*
10	502	00 43 43.9	−09 04 23	–	17.30	0.340	9.73	15004	15038	182	11.8	−0.33	−0.19	2.03	*N*

Notes. Column (1): Sequence ID number.
Column (2): [DFL98] galaxy name (Durret et al. 1998); ([a]) [SDG98] galaxy name (Slezak et al. 1998); and ([b]) PGC names (Paturel et al. 1989).
Columns (3) and (4): RA, Dec. coordinates from NED.
Column (5): The morphological type from NED, except (*) taken from HyperLEDA.
Columns (6) and (7): The g magnitude and $(g-r)$ colour index estimated in this work from CFHT/PanSTARRS images.
Column (8): Stellar mass given by $\log(M_*/M_\odot)$.
Column (9): Optical velocity from our redshift membership catalogue (see Section 2).
Column (10): Heliocentric HI velocity. The uncertainty is taken as one-half the velocity resolution, i.e. $\sim$23 $km\,s^{-1}$ (see Table 3).
Column (11): The galaxy velocity width, the uncertainty is $\sim$46 $km\,s^{-1}$ (see Table 3).
Column (12): The HI-Mass following Haynes & Giovanelli (1984); uncertainties are lower than 10%; see the text for more details.
Columns (13) and (14): The upper and lower limits for HI deficiency, following Haynes & Giovanelli (1984).
Column (15): The projected cluster-centric distance considering the position of the corresponding BCG.
Column (16): Qualitative code indicating if the galaxy is normal in HI (N), otherwise it is perturbed. See the text for more details.

Downloaded from https://academic.oup.com/mnras/article/517/1/1218/6694106 by CNRS user on 13 April 2023

Table A2. The HI detected galaxies in Abell 496.

ID (1)	Name (2)	RA (2000) (3)	Dec. (2000) (4)	Morph. type (5)	g mag (6)	colour $(g-r)$ (7)	M_* (8)	Opt-vel km s^{-1} (9)	HI-vel km s^{-1} (10)	Δv km s^{-1} (11)	M_{HI} 10^9 M$_\odot$ (12)	Def_{HI} Sa-Sb (13)	Def_{HI} Sc-Irr (14)	Dist. Mpc (15)	HI pert. (16)
1	603	04 30 49.8	−13 12 28	–	16.92	0.193	9.29	9786	9724	88	1.7	−0.19	−0.11	1.63	*N*
2	672	04 31 03.4	−13 11 21	Sc	17.69	0.302	8.99	10776	10783	177	2.3	−0.14	−0.04	1.51	*N*
3	B042910.53−130437.3	04 31 30.0	−12 58 15	–	18.83	0.272	8.44	–	10407	44	1.9	−1.00	−0.97	1.42	*N*
4	853	04 31 32.0	−13 14 34	–	17.14	0.278	9.23	9208	9264	219	2.6	−0.22	−0.12	1.22	*N*
5	903***	04 31 40.3	−13 07 11	–	17.48	0.455	9.18	10904	–	–	>2.3	–	–	1.19	
6	926***	04 31 43.1	−13 07 10	–	17.08	0.596	9.44	11106	–	–	>1.0	–	–	1.16	
7	958	04 31 47.7	−12 44 23	–	19.38	0.224	8.16	–	10186	132	0.8	−0.16	−0.10	1.64	*N*
8	982	04 31 50.3	−12 43 54	–	17.68	0.174	8.93	10919	10871	89	1.0	−0.14	−0.06	1.64	*N*
9	989	04 31 51.8	−13 07 43	–	18.96	0.288	8.39	10006	10275	221	3.3	−0.38	−0.28	1.08	*Vel*
10	1054	04 32 02.8	−13 29 48	I	16.73	0.464	9.53	10289	9329	175	1.5	−0.03	0.07	1.08	*Vel, Pos*
11	1099	04 32 09.6	−12 41 42	Sc	15.70	0.584	10.07	10323	10319	309	7.3	−0.07	0.08	1.60	*N*
12	1169	04 32 20.4	−13 14 11	Sb	16.39	0.401	9.65	8990	8979	262	8.9	−0.52	−0.41	0.76	*N*
13	1179	04 32 21.8	−13 15 48	–	17.55	0.371	9.10	10057	10076	176	1.4	−0.15	−0.06	0.74	*N*
14	1275	04 32 41.8	−13 03 21	–	19.10	0.349	8.36	10608	10473	88	1.0	−0.17	−0.10	0.73	*Vel*
15	04.56-13.38**	04 32 45.3	−13 23 08	–	21.12	0.296	7.39	–	10694	88	0.6	−0.11	−0.05	0.59	*N*
16	1303	04 32 45.5	−12 33 39	–	19.68	0.399	8.12	–	9264	44	3.5	−1.20	−1.16	1.75	*N*
17	1315	04 32 48.1	−12 42 52	–	16.36	0.191	9.55	9954	9615	132	3.6	−0.17	−0.06	1.39	*Vel, Asy*
18	1324	04 32 49.0	−12 42 19	–	18.09	0.254	8.78	10037	9615	132	1.1	−0.16	−0.09	1.41	*Vel, Asy*
19	1338	04 32 51.1	−13 03 07	–	18.92	0.320	8.43	10474	10473	88	1.1	−0.33	−0.27	0.68	*N*
20	1354	04 32 54.2	−13 23 50	–	17.16	0.498	9.35	9932	9922	220	3.6	−0.62	−0.54	0.53	*N*
21	1363	04 32 54.7	−12 53 25	–	18.11	0.250	8.77	–	10385	88	2.5	−0.49	−0.41	0.98	*N*
22	04.55-13.06**	04 32 55.4	−13 03 33	–	21.33	0.484	7.40	–	10429	88	1.0	−0.78	−0.75	0.64	*N*
23	198[c]	04 32 56.1	−13 36 38	Sc	15.65	0.709	10.16	11349	10561	177	2.5	−0.16	−0.06	0.92	*Vel*
24	3760	04 32 56.8	−12 46 41	SBbc	15.23	0.745	10.37	10602	10606	354	5.3	0.14	0.29	1.22	*Asy*
25	1386	04 32 59.8	−13 42 33	–	16.95	0.739	9.57	10557	10473	265	3.1	−0.10	0.01	1.13	*Asy*
26	1389	04 33 00.1	−13 57 28	–	19.65	0.535	8.21	–	10186	44	1.4	−0.71	−0.66	1.70	*N*
27	1399	04 33 02.0	−12 43 00	–	15.79	0.457	9.96	9361	9373	263	5.4	−0.59	−0.49	1.35	*N*
28	1418	04 33 05.3	−13 26 55	–	18.42	0.472	8.75	–	10473	89	1.2	−0.12	−0.03	0.55	*N*
29	1419	04 33 05.9	−13 59 54	–	18.84	0.860	8.75	10943	10971	266	1.6	0.36	0.47	1.79	*Def*
30	1457	04 33 10.9	−13 14 10	–	17.79	0.495	9.05	8991	8914	131	1.8	−0.32	−0.24	0.27	*Pos*
31	1461	04 33 11.4	−13 28 02	–	18.14	0.461	8.87	10670	10650	177	2.8	−0.54	−0.46	0.55	*N*
32	1474	04 33 13.7	−13 27 56	–	18.94	0.415	8.47	10159	10120	88	1.1	−0.31	−0.25	0.54	*N*
33	1482	04 33 15.1	−13 21 19	–	18.04	0.317	8.83	10207	10186	132	0.8	0.03	0.11	0.31	*N*
34	225[c]	04 33 17.4	−12 59 01	Sb	15.61	0.674	10.16	10826	10915	266	0.6	0.35	0.44	0.70	*Def*
35	1512	04 33 19.6	−13 33 39	–	19.20	0.358	8.32	10268	10253	88	0.7	−0.17	−0.10	0.74	*N*
36	1547	04 33 23.3	−13 20 21	Sc	16.89	0.504	9.48	10188	10208	265	3.8	−0.27	−0.17	0.23	*N*
37	1549	04 33 23.9	−13 31 03	S	16.74	0.590	9.59	10228	10231	397	10.4	−0.75	−0.64	0.63	*N*
38	1565	04 33 25.4	−13 41 09	Sc	16.75	0.524	9.55	10866	10827	354	3.1	−0.12	0.00	1.02	*Pos*
39	1584	04 33 29.0	−13 41 15	–	20.40	0.273	7.72	9443	9527	44	0.4	0.31	0.39	1.02	*Def*
40	1624	04 33 34.6	−12 38 34	–	19.40	0.329	8.21	–	10539	133	1.4	−0.22	−0.14	1.48	*N*
41	1656***	04 33 38.5	−13 35 46	I	16.98	0.411	9.38	11194	–	–	>0.9	–	–	0.80	
42	1709	04 33 44.7	−13 33 50	I	17.07	0.523	9.40	9779	9724	176	1.2	0.23	0.33	0.72	*Def, Pos*

Downloaded from https://academic.oup.com/mnras/article/517/1/1218/6694106 by CNRS user on 13 April 2023

Table A2 – *continued*

ID (1)	Name (2)	RA (2000) (3)	Dec. (2000) (4)	Morph. type (5)	g mag (6)	colour $(g-r)$ (7)	M_* (8)	Opt-vel km s^{-1} (9)	HI-vel km s^{-1} (10)	Δv km s^{-1} (11)	M_{HI} 10^9 $M_\odot$ (12)	Def_{HI} Sa-Sb (13)	Def_{HI} Sc-Irr (14)	Dist. Mpc (15)	HI pert. (16)
43	1747***	04 33 50.9	−13 44 18	–	18.62	0.400	8.61	11037	–	–	>0.8	–	–	1.15	
44	1834	04 34 02.0	−13 17 49	Sbc	15.89	0.470	9.92	10347	10319	132	2.3	−0.01	0.10	0.25	*N*
45	1849	04 34 04.1	−12 48 52	–	18.56	0.356	8.62	9002	9023	88	1.1	−0.02	0.07	1.10	*N*
46	1860***	04 34 06.3	−13 39 44	–	19.40	0.476	8.29	11267	–	–	>1.8	–	–	1.00	
47	1967	04 34 23.9	−13 15 32	–	18.16	0.405	8.83	9480	9483	132	0.7	0.08	0.15	0.45	*N*
48	2036	04 34 36.8	−12 45 30	–	19.08	0.128	8.25	9936	9944	88	1.5	−0.49	−0.43	1.33	*N*
49	2246	04 35 10.5	−13 59 34	–	18.01	0.685	9.03	–	10451	132	3.0	−0.56	−0.48	1.96	*N*
50	2252	04 35 11.0	−13 45 18	–	17.97	0.446	8.94	10963	11004	87	2.9	−0.32	−0.23	1.49	*N*
51	B043258.99−130504.4	04 35 18.3	−12 58 58	–	20.78	0.554	7.70	–	10054	44	1.3	−0.47	−0.41	1.18	*N*
52	2447	04 35 45.5	−13 58 37	–	17.86	0.694	9.09	–	10606	265	4.3	−0.34	−0.24	2.11	*Asy*
53	2485	04 35 52.0	−13 19 47	Sab	16.10	0.810	10.00	10301	10363	309	1.4	0.43	0.55	1.31	*Def, Pos*
54	2503	04 35 54.5	−13 34 49	S0-a	19.29	0.472	8.34	–	10385	88	0.8	−0.53	−0.49	1.53	*N*
55	2516	04 35 56.7	−13 19 49	–	18.70	0.331	8.54	10609	10584	133	1.0	−0.11	−0.03	1.36	*N*
56	2525	04 35 57.8	−13 43 56	–	19.65	0.604	8.25	–	10385	177	1.3	−0.15	−0.07	1.76	*N*
57	2534	04 35 59.5	−13 18 07	Sab	16.06	0.830	10.03	10188	10098	220	0.9	0.55	0.67	1.38	*Def*
58	04.60–13.55**	04 36 14.2	−13 33 20	–	–	–	–	–	10960	44	0.8	−0.76	−0.73	1.66	*N*

Notes. Column (1): Sequence ID number.
Column (2): [SDG99]-SRC galaxy name (Slezak et al. 1999); ([c]) [DFL99] galaxy name (Durret et al. 1999); (**) The names were constructed using RA, Dec. in hours, and decimal degrees, they are objects not catalogued in NED, and the coordinates shown for these objects are those of the HI emission. (***) The emission extends beyond the observed range.
Columns (3) and (4): RA, Dec. coordinates from NED.
Column (5): The morphological type from NED.
Columns (6) and (7): The g magnitude and $(g-r)$ colour index estimated in this work from CFHT/PanSTARRS images.
Column (8): Stellar mass given by $\log(M_*/M_\odot)$
Column (9): Optical velocity from our redshift membership catalogue (see Section 2).
Column (10): Heliocentric HI velocity. The uncertainty in taken as one-half the velocity resolution, i.e. ∼22 km s^{-1} (see Table 3).
Column (11): The galaxy velocity width, the uncertainty is ∼44 km s^{-1} (see Table 3).
Column (12): The HI-Mass following Haynes & Giovanelli (1984); uncertainties are lower than 10 per cent; see the text for more details.
Columns (13) and (14): The upper and lower limits for HI deficiency, following Haynes & Giovanelli (1984).
Column (15): The projected cluster-centric distance considering the position of the corresponding BCG.
Column (16): Qualitative code indicating the HI appearance, either normal or perturbed. See the text for more details.

Downloaded from https://academic.oup.com/mnras/article/517/1/1218/6694106 by CNRS user on 13 April 2023

Table A3. The HI detected galaxies in Abell 2670.

ID	Name	RA (2000)	Dec (2000)	Morph. type	g mag	colour $(g-r)$	M_*	Opt-vel km s^{-1}	HI-vel km s^{-1}	Δv km s^{-1}	M_{HI} 10^9 $M_\odot$	Def_{HI} Sa-Sb	Def_{HI} Sc-Irr	Dist. Mpc	HI pert.
(1)	(2)	(3)	(4)	(5)	(6)	(7)	(8)	(9)	(10)	(11)	(12)	(13)	(14)	(15)	(16)
1	J235222.31−104134.7	23 52 22.3	−10 41 35	–	19.03	0.364	9.28	22814	22666	238	5.4	−0.47	−0.36	2.81	*Vel, Pos*
2	J235232.39−104154.1	23 52 32.4	−10 41 54	–	19.35	0.249	9.07	–	22595	95	4.4	−0.57	−0.48	2.65	*N*
3	J235233.13−103640.8	23 52 33.1	−10 36 41	–	18.34	0.388	9.62	22724	22690	191	4.8	−0.35	−0.24	2.40	*Pos*
4	J235247.36−105259.1	23 52 47.3	−10 52 59	E?*	16.78	0.640	10.51	22721	22714	143	6.6	0.19	0.35	3.08	*Def, Pos*
5	3325027[b]	23 52 55.8	−10 42 04	–	19.16	0.354	9.21	21795	21929	95	2.6	−0.20	−0.10	2.24	*N*
6	J235303.74−110454.9	23 53 03.7	−11 04 55	S?*	16.30	0.679	10.76	22823	22738	191	7.0	−0.01	0.14	3.82	*N*
7	J235305.67−104055.6	23 53 05.7	−10 40 56	Sbc	16.51	0.434	10.49	21930	21953	427	14.4	−0.31	−0.17	2.02	*N*
8	J235308.87−104417.3	23 53 08.9	−10 44 17	E?	17.96	0.802	10.06	22578	22547	667	25.6	−0.60	−0.46	2.19	*N*
9	J235310.49−104142.3	23 53 10.5	−10 41 42	–	20.00	0.267	8.78	–	21858	142	3.6	−0.79	−0.72	2.00	*N*
10	J235310.87−110203.0	23 53 10.9	−11 02 03	S?*	17.33	0.684	10.29	22806	22785	96	3.4	0.12	0.25	3.52	*Def*
11	J235319.07−102303.2	23 53 19.1	−10 23 03	Sc	17.07	0.614	10.36	22300	22305	236	4.2	0.13	0.27	1.19	*Def*
12	J235320.90−101047.7	23 53 20.9	−10 10 48	–	18.67	0.352	9.44	22306	22423	283	2.7	−0.06	0.05	1.70	*N*
13	2dFGRS S888Z177	23 53 20.9	−10 32 39	–	19.14	0.445	9.28	23114	23298	142	3.0	−0.29	−0.20	1.31	*Vel*
14	J235324.23−104916.6	23 53 24.2	−10 49 17	–	17.70	0.330	9.88	21947	21976	190	7.1	−0.67	−0.58	2.38	*Pos, Asy*
15	J235326.38−101549.0	23 53 26.4	−10 15 49	E?*	18.22	0.603	9.82	22410	22399	425	12.6	−0.11	0.04	1.31	*N*
16	J235338.22−105443.9	23 53 38.2	−10 54 44	S?*	17.47	0.589	10.16	22484	22476	143	6.7	−0.22	−0.09	2.71	*Pos*
17	J235339.45-102430.1	23 53 39.4	−10 24 30	–	20.11	0.302	8.74	–	22588	142	2.6	−0.44	−0.35	0.72	*N*
18	J235339.87−102547.6	23 53 39.9	−10 25 48	Sa	17.26	0.552	10.23	22552	22612	189	2.6	0.16	0.28	0.73	*Def, Pos*
19	J235341.02−103453.9	23 53 41.0	−10 34 54	–	19.93	0.375	8.87	–	21482	188	3.2	−0.57	−0.49	1.11	*N*
20	J235344.08−104041.2	23 53 44.1	−10 40 41	–	20.54	0.544	8.70	–	23575	48	2.1	−0.51	−0.45	1.51	*N*
21	J235346.66−101614.8	23 53 46.7	−10 16 15	Sab	16.31	0.629	10.73	23796	23964	143	3.7	0.36	0.52	0.97	*Def, Vel, Pos*
22	J235356.57−101510.4	23 53 56.6	−10 15 10	Sd	17.07	0.495	10.28	21565	21529	94	2.2	−0.51	−0.44	0.94	*N*
23	141225[b]	23 53 57.1	−10 22 29	Sa	17.31	0.509	10.17	21898	21834	423	10.6	−0.46	−0.33	0.43	*N*
24	141233[b]	23 53 58.5	−10 28 27	–	19.26	0.360	9.17	22168	22140	283	5.0	−0.56	−0.47	0.44	*N*
25	J235411.73−102115.1	23 54 11.7	−10 21 15	–	19.26	0.375	9.18	24268	24321	95	2.3	−0.30	−0.21	0.35	*N*
26	J235413.59−102748.2	23 54 13.6	−10 27 48	E?	17.79	0.563	9.99	24568	24536	143	1.7	0.03	0.14	0.24	*N*
27	J235418.24−101349.5	23 54 18.2	−10 13 50	Sc	17.43	0.580	10.17	23251	23227	474	11.0	0.08	0.25	1.00	*Def*
28	J235419.51−103300.3	23 54 19.5	−10 33 00	Sa	16.77	0.601	10.49	23925	23964	429	11.5	−0.25	−0.11	0.71	*Asy, Pos*
29	J235435.77−095748.6	23 54 35.8	−09 57 49	S?*	17.94	0.370	9.79	23442	23407	144	9.2	−0.30	−0.17	2.46	*N*
30	J235438.15−101907.6	23 54 38.1	−10 19 08	Sab	16.76	0.523	10.44	22506	22517	378	10.0	−0.19	−0.05	0.75	*Asy*
31	J235444.17−101655.9	23 54 44.2	−10 16 56	Scd	17.00	0.426	10.26	23184	23120	383	7.3	−0.01	0.14	0.98	*Pos*
32	J235446.43−095752.9	23 54 46.4	−09 57 53	–	17.73	0.780	10.16	22768	22666	334	4.6	−0.05	0.07	2.50	*N*
33	J235449.71−100151.0	23 54 49.7	−10 01 51	–	18.43	0.466	9.63	–	21857	237	2.7	0.36	0.50	2.20	*Def, Pos*

Downloaded from https://academic.oup.com/mnras/article/517/1/1218/6694106 by CNRS user on 13 April 2023

Table A3 – *continued*

ID	Name	RA (2000)	Dec (2000)	Morph. type	g mag	colour $(g-r)$	M_*	Opt-vel km s^{-1}	HI-vel km s^{-1}	Δv km s^{-1}	M_{HI} 10^9 M$_\odot$	Def_{HI} Sa-Sb	Def_{HI} Sc-Irr	Dist. Mpc	HI pert.
(1)	(2)	(3)	(4)	(5)	(6)	(7)	(8)	(9)	(10)	(11)	(12)	(13)	(14)	(15)	(16)
34	J235451.55−101238.9	23 54 51.5	−10 12 39	–	19.13	0.253	9.17	23284	23216	191	3.2	−0.27	−0.17	1.37	*N*
35	J235453.62−101931.6	23 54 53.6	−10 19 32	Im	18.13	0.505	9.79	21818	21787	235	4.5	−0.24	−0.12	0.99	*Pos*
36	J235454.17−101717.0	23 54 54.2	−10 17 17	Sc	15.83	0.544	10.89	23065	23168	478	10.9	−0.01	0.15	1.12	*Asy*
37	J235607.62−095938.1	23 56 07.6	−09 59 38	E*	17.00	0.670	10.43	23035	23168	96	2.8	0.31	0.44	3.34	*Def, Pos*
38	J235619.93−101246.2	23 56 19.9	−10 12 46	S?*	16.23	0.507	10.67	22923	22953	430	10.2	−0.20	−0.06	2.95	*N*

Notes. Column (1): Sequence ID number.
Columns (2): SDSS names; (^{b}) PGC names (Paturel et al. 1989).
Columns (3) and (4): RA, Dec. coordinates from NED.
Column (5): The morphological type from NED, except (*) taken from HyperLEDA.
Columns (6) and (7): The g magnitude and $(g-r)$ colour index estimated in this work from CFHT/PanSTARRS images.
Column (8): Stellar mass given by $\log(M_*/M_\odot)$.
Column (9): Optical velocity from our redshift membership catalogue (see Section 2).
Column (10): Heliocentric HI velocity. The uncertainty in taken as one-half the velocity resolution, i.e. ∼24 km s^{-1} (see Table 3).
Column (11): The galaxy velocity, the uncertainty is ∼48 km s^{-1}(see Table 3).
Column (12): The HI-Mass following Haynes & Giovanelli (1984); uncertainties are lower than 10%; see the text for more details.
Columns (13) and (14): The upper and lower limits for HI deficiency, following Haynes & Giovanelli (1984).
Column (15): The projected cluster-centric distance considering the position of the corresponding BCG.
Column (16): Qualitative code indicating the HI appearance, either normal or perturbed. See the text for more details.

This paper has been typeset from a TEX/LATEX file prepared by the author.

Downloaded from https://academic.oup.com/mnras/article/517/1/1218/6694106 by CNRS user on 13 April 2023